Mathematics

AIMS Mathematics, 11(7): 22807–22844.
DOI: 10.3934/math.2026920
Received: 24 January 2026
Revised: 30 June 2026
Accepted: 08 July 2026
Published: 28 July 2026

https://www.aimspress.com/journal/Math

Research article

Data-driven intelligent framework for energy optimization viscoelastic hybrid nanofluid over a permeable surface with heterogeneous-homogeneous reactions

Fisal Asiri*

Department of Mathematics, Taibah University, Medina 42353, Saudi Arabia

* **Correspondence:** Email: fahasiri@taibahu.edu.sa.

Abstract: Viscoplastic hybrid nanofluids (HNFs) have demonstrated significant potential as working fluids in technological and industrial applications, such as energy-effective heat exchangers, polymer extrusion, catalytic chemical reactors, and biomedical membrane transfer. Convective thermal conditions, reactive species movement, and yield stress rheology all concurrently control the overall process efficiency and product quality in these systems. The boundary layer flow literature has not adequately addressed the precise characterization of heat and mass transport behavior in such multi-physics arrangements over stretched surfaces embedded in porous media, despite their practical significance. For the first time, the two-dimensional Darcy-Forchheimer dissipative flow of a Papanastasiou-Bingham HNF with shape-specific CNT (platelet, shape factor 5.7) and Al_2O_3 (spherical, shape factor 3.0) nanoparticles distributed in dihydrogen as base fluid over a convectively heated stretching surface embedded in a porous medium was investigated in this work. Forchheimer inertia dissipation was directly incorporated into the energy equation to physically represent frictional heating in the porous matrix. The regulating flow equations as a set of partial differential equations (DEs) were transformed into ordinary DEs. An artificial neural network (ANN) was developed using eight different training functions for predicting flow, temperature, and concentration. I found that the mixed convection due to a H-H reaction amplified the flow and energy profile, while conflicting behavior was seen for concentration. The viscoplastic fluid containing hybrid nanoparticles uplifted the wall stress, heat, and mass fluxes. The temperature of Papanastasiou-Bingham HNF was much higher than Papanastasiou-Bingham fluid. Moreover, the wall shear stress increased with Darcy and Bingham factors.

Keywords: mixed convection; Levenberg-Marquardt (LM) backpropagation ANN; Papanastasiou-Bingham fluid model; CNT-Al_2O_3 nanomaterials; Heterogeneous-Homogeneous chemical reaction
Mathematics Subject Classification: 80A05

Nomenclature

Symbol	Description	SI Unit
u, v	Velocity components in x- and y-directions	$m \cdot s^{-1}$
x, y	Cartesian coordinates	m
T	Temperature of the fluid	K
T_∞	Ambient temperature	K
T_w	Wall temperature	K
C_1, C_2	Concentration of chemical species A and B	mol$\cdot m^{-3}$
$C_{1\infty}$	Ambient concentration of species A	mol$\cdot m^{-3}$
a_∞	Reference concentration of species A	mol$\cdot m^{-3}$
p	Fluid pressure	Pa
k_{Hnf}	Thermal conductivity of hybrid nanofluid	$W.m^{-1}.K^{-1}$
k_f	Thermal conductivity of base fluid	$W.m^{-1}.K^{-1}$
g	Gravitational acceleration	$m \cdot s^{-2}$
D_A, D_B	Diffusion coefficients of species A and B	$m^2 \cdot s^{-1}$
k_1	Homogeneous reaction rate constant	$m^6.mol^{-1} \cdot s^{-1}$
k_2	Heterogeneous reaction rate constant	$m \cdot s^{-1}$
K^*	Porous medium permeability	m^2
C_d	Forchheimer inertia drag coefficient	m^{-1}
H_F	Convective heat transfer coefficient	$W.m^{-1}.K^{-1}$
a	Stretching rate constant	s^{-1}
u_w	Stretching wall velocity	$m \cdot s^{-1}$
f	Dimensionless stream function	—
f'	Dimensionless velocity profile	—
$G(\eta)$	Dimensionless concentration of species A	—
$H(\eta)$	Dimensionless concentration of species B	—
$\Theta(\eta)$	Dimensionless temperature profile	—
C_f	Skin friction coefficient	—
Nu_x	Local Nusselt number	—
Sh_x	Local Sherwood number	—
$Bn = \frac{\tau_y^*}{\mu_f c}$	Bingham number	
$n^* = cn$	Growth parameter	—
$Re_x = \frac{ax^2}{v_f}$	Reynold number	—

Continued on next page

Symbol	Description	SI Unit
$Re_x = \frac{ax^2}{v_f}$	Reynold number	—
$D_a = \frac{v_f}{aK^*}$	Darcy number	—
$F_r = \frac{C_d}{\sqrt{K^*}}$	Forchheimer parameter	—
$Pr = \frac{\mu_f c_p}{k_f}$	Prandtl number	—
$Ec = \frac{(u_w)^2}{c_p(T_w - T_\infty)}$	Eckert number	—
$Nr = \frac{4\sigma^* \bar{T}_\infty^3}{\kappa^* k_f}$	Radiative parameter	—
$Sc = \frac{v_f}{D_B}$	Schmidt number	—
$K_r = \frac{\bar{k}_1 \bar{a}_\infty^2}{c}$	Homogenous reaction rate parameter	—
$K_S = \frac{\bar{k}_2}{D_A}\sqrt{\frac{c}{v_f}}$	Heterogeneous reaction rate parameter	—
$\beta = \frac{D_B}{D_A}$	Diffusion ratio coefficient	—
$\lambda_m = \frac{Gr_T}{Re_x^2}$	Mixed convection parameter	—
$Gr_T = \frac{u_w \delta_T (\bar{T} - \bar{T}_\infty) g}{v_f^2}$	Thermal Grashof number	—
$\gamma_1 = \frac{u_w \delta_{\bar{C}_1} (\bar{C}_1 - \bar{C}_{1\infty})) g}{v_f^2}$	Solutal Grashof number due to Homogenous reaction	—
$\gamma_2 = \frac{u_w \delta_{\bar{C}_2} (\bar{C}_2 - \bar{C}_{2\infty})) g}{v_f^2}$	Solutal Grashof number due to Heterogeneous reaction	—
ANN	Artificial Neural Network	—
LM	Levenberg-Marquardt	—
LMB-ANN	Levenberg-Marquardt Backpropagation Artificial Neural Network	—
RKF-45	Runge-Kutta-Fehlberg Fourth-Fifth Order Method	—
MSE	Mean Squared Error	—
RMSE	Root Mean Squared Error	—
HNF	Hybrid Nanofluid	—
NF	Nanofluid	—
BL	Boundary Layer	—

Continued on next page

Symbol	Description	SI Unit
H-H	Heterogeneous-Homogeneous	—
MHD	Magnetohydrodynamics	—
CNT	Carbon Nanotube	—
ODE	Ordinary Differential Equation	—
PDE	Partial Differential Equation	—
2D	Two-Dimensional	—

1. Introduction

The non-Newtonian fluids have been studied in great detail because of their complicated behavior and industrial uses [1,2]. These fluids' nonlinear interactions between applied force and fluid properties are part of their structure. Comprehending the dynamics of non-Newtonian fluids becomes challenging due to this nonlinearity. Various models pertaining to such fluids have been suggested to achieve this goal. A fundamental idealized group of non-Newtonian materials has a yield stress that needs to be surpassed for there to be noticeable deformation. These consist of doughs, slurry, and oils, and they can withstand applied force when at rest. Based on experimental observation and empiricism, non-Newtonian models have been put out to forecast the rheological behavior of such materials. For many years, the functioning of lubricants, especially greases, has been described using the Bingham plastic model [3] having non-Newtonian fluid flow behavior. Additionally, it has been used to explain how melts and slurries move through molds and during chemical treatment. The yield shear stress and viscosity are the two factors that define the Bingham model. The material is stiff when the deviatoric stress tensor magnitude is smaller than the yield stress; when the yield stress is greater, the material flows in a way that is almost Newtonian. The size of the deformation rate in two-dimensional thin-film flow is directly proportional to the distinction between the yield shear stress and the shear stress. The optimal Bingham constitutive equations have been given as [4] to model the deformation-stress dynamics of Bingham fluids [5].

$$\hat{\tau} = \hat{\tau}_0 + \mu_p \tilde{\gamma}\text{: if } |\hat{\tau}| > \hat{\tau}_0, \tag{1}$$

$$\tilde{\gamma} = 0\text{: if } |\hat{\tau}| \leq \hat{\tau}_0. \tag{2}$$

Here, $\hat{\tau}$, $\hat{\tau}_0$, $\tilde{\gamma}$, and μ_p are the Cauchy stress tensor, yield stress, shear rate tensor, and constant plastic viscosity, respectively. The material turns into solid (unyielded region) when the shear stress $\hat{\tau}$ descends below $\hat{\tau}_0$, as determined by these constitutive characteristics. To get around the viscoplastic model's intrinsic instability, Papanastasiou [6] suggested a modified equation that causes the shear stress to fluctuate consistently with the shear rate. Moreover, yielding and unyielding regions can use the equation owing to the so-called normalization procedure. The Bingham model is transformed into Eq (3) by the Papanastasiou exponential transformation.

$$\hat{\tau} = \mu_{app} \mathcal{A}_1 = \left(\mu_f + \frac{\hat{\tau}_0}{|\dot{\tilde{\gamma}}|} \left(1 - e^{-n\tilde{\gamma}}\right) \right) \mathcal{A}_1. \tag{3}$$

Here, n signify transition among yielded and un-yielded region. For $n \rightarrow 0$, the classical viscous fluid is attained. μ_f, μ_{app} are the dynamics and apparent viscosity, respectively, $\mathcal{A}_1$ is the deformation, and n is the regularization parameter. $\mathcal{A}_1$ is the deformation rate product [7].

$$\mathcal{A}_1 = grad\vec{V} + grad(\vec{V})^t \text{ and } \tilde{\gamma} = \sqrt{\left(\frac{1}{2}\right) trac\mathcal{A}_1^2}. \quad (4)$$

The chemical processes can be roughly categorized as either heterogeneous (H) or homogeneous (H) in nature. In systems with evenly combined reactants and catalysts that reside in the same phase, homogeneous reactions occur [8,9]. On the other hand, heterogeneous processes like rechargeable battery reactions, metal-acid associations, degradation procedures, and electrolytic cells take place at the intersections between distinct phases [10]. Biochemical systems, combustion, ignition, and catalytic conversions are only a few examples of the numerous natural and commercial processes that use homogeneous and heterogeneous dynamics. Catalyst presence is usually necessary for heterogeneous reactions, such as those that occur in food processing, distillation, hydrometallurgical activities, polymer production, and fog creation [11].

Mathematically, the H-H reactions are defined as [12]:

$$\mathcal{A} + 2\mathcal{B} \rightarrow 3\mathcal{B}, \text{ rate } = \bar{k}_1\bar{a}\bar{b}^2, \quad (5)$$

$$\mathcal{A} \rightarrow \mathcal{B}, \text{ rate } = \bar{k}_2\bar{a}. \quad (6)$$

Here, $\bar{a}$ and $\bar{b}$ are the concentration of chemical types $\mathcal{A}$ and $\mathcal{B}$, respectively. $\bar{k}_i$ $(i = 1,2)$.

Ramzan et al. [13] examined the influence of H-H on nanofluid (NF) flow in a permeable channel. They investigated the effects of adding symmetric H-H reactions and heat absorption/generation, respectively, on the NF flow in a porous channel containing a Go −water composition. Entropy generation due to H-H reactions and nanomaterial was explored by Hashim et al. [14]. Their results indicated that an upward trend for the productive parameter and a decrease in the concentration gradient are caused by raising the values of the negative chemical reaction rate parameter. Feng and Su [15] examined the artificial chemistry in flow, unlocking transitioning from Photolysis and H-H reactions. They provided an overview of current developments in photolytic and photocatalytic artificial chemistry carried out in flow systems, with a particular emphasis on heterogeneous photocatalysis, particularly from the standpoint of the construction of reactors. Various flow system benefits and drawbacks were examined, along with some useful design strategy considerations. Jena et al. [16] scrutinized the 3D, MHD revolving flow of radiated NF over a stretchable sheet with H-H reactions. They concluded that as the values of H-H parameters increase, the concentration of NF decreases.

Common fluids are widely used in many heat transfer devices, such as solar collectors, chemical manufacturing in the energy sector, avionic and automobile cooling mechanisms, and heating in the textile industry, among others [17,18]. Increasing the thermal conductivity of common liquids can improve the efficiency of these devices. Choi and Eastman [19] investigated the suspension of nanoparticles in ordinary liquids. Furthermore, various methods have been used to improve heat transfer and reduce energy losses. Increasing the thermal conductivity of the working fluid is the newest and most effective method of thermal enhancement. The most recent technique makes use of distributed solid nanoparticles. Moreover, NFs are fluids that contain nanoparticles. Thermal transfer is significantly improved by NFs. Hybrid NF (HNF) is a sophisticated kind of NF that is created by dispersing two or more nanomaterials in a base liquid. According to research [20–22], the HNFs provide cooling systems with optimal viscosity and higher thermal efficiency. HNFs are a new type of NF that were created. The fossil fuel business, energy collecting devices, optical energy production, metallic furnaces, chilling media, polymeric molding, and manufacturing techniques are only a few of the many uses for these materials. Two or three nanoparticle metals, carbides, oxides, and carbon nanotubes combine to form the mixture. HNFs have better information on the thermal behavior of heat transfer equipment than NFs. Muneeshwaran et al. [23] explored the role of hybrid nanomaterials on the heat transfer improvement. They discussed the hydrothermal behavior of HNF in a range of heat transfer applications, including refrigeration systems, assault jet cooling, stored thermal energy, thermal energy storage, heat pumps, heat conduits, solar energy systems, natural convection cavities and enclosures, and boiling-associated applications. Sarkar et al. [24] uncovered developments and progress in HNFs for advance heat transfer applications. Some significant developments for HNFs and their promising applications are presented in [25–27].

The ability of Artificial Neural Networks (ANNs) to describe and solve extremely complex, rigid, and nonlinear mathematical problems has led to their growing use as computing tools throughout the last ten years. They are particularly helpful in many domains, such as computational fluid dynamics, mathematical biology, and biological research, due to their ease of use and versatility. Unlike traditional computing techniques, ANNs are able to learn from data, identify complex patterns, and generalize solutions without the need for pre-programmed code. Because of their significant applications, they are regarded as a significant enabler in a number of industrial setups, containing microelectronics, medicine, medical technology, and transportation networks, especially in fields like tissue engineering, heat transfer modeling, and precision drug administration [28–30]. ANNs are composed of interconnected neurons that process and transform disorganized input data into ordered outputs, inspired from the structure and functions of the brain. By adapting and learning from fresh data, prediction capacity is progressively enhanced. As network complication increases with additional neurons and layers, their prediction efficiency improves, making them highly expandable and suitable for a wide range of applications. An efficient Levenberg–Marquardt (LM) backpropagation technique is one of numerous training methods that have been demonstrated to be especially effective in preserving convergence and enhancing the caliber of solutions for complex automated networks. There has been a significant advancement in the applications of ANNs in fluid dynamics simulations. For instance, Akbar et al. [31] simulated the HNF flow with convective boundary conditions through a permeable stretched sheet through a LM backpropagated ANN approach. Investigations of transition states, analysis of regression, mean square error, and error histogram studies were conducted to substantiate the effectiveness of the proposed ANN for solving the HNF flow. Achieving a high degree of precision within the range of 10^{-6} to 10^{-8}, the constant compatibility of the obtained findings with matching solutions attests to the validity of the structure. The characteristics of magnetohydrodynamics (MHD) and heat transfer in a HNF flow past a wedge-shaped artery using ANN were conducted by Shah et al. [32]. Alimi et al. [33] implemented the computational and ANN approach to estimate the HNF and heat transfer features with Cattaneo-Christov theory. They concluded that precision of ANN lies in a range of 10^{-8} to 10^{-9}. The groundbreaking potential of ANNs as optimization and prediction methods in modern engineering and science is demonstrated by these developments, particularly when it comes to handling difficult problems where conventional computational methods are limited.

1.1. Motivation and application of my research

- **Applications of HNF:** There are several applications for simulating HNF flow with convective boundary conditions across a porous stretched sheet in industrial domain and real-world engineering domains. Enhancement of heat transfer could be used in a number of industries where effective heat transfer is essential, including heat exchanges in chemical processes, air conditioning systems in cars, and temperature management in electronics. The development of renewable energy systems may benefit from an understanding of convective boundary conditions and heat transport across porous media. This research may help develop more effective solar collectors or solar thermal power systems for solar energy applications.
- **Intelligence based system applications:** The development of layered recurrent intelligence-based prediction using LMB-ANN is used to forecast complex Bingham HNF flow, especially in the deployment of three nanomaterials, Al_2O_3, and CNT.
- **Optimization of heat transfer for industrial extending sheets:** Many industrial uses include sheet expansion, while investigations into the effects of HNF under radiation during stretching may lead to more effective manufacturing techniques.
- **Application of H-H chemical in nanofluidic devices:** There are several uses for H-H chemical interactions, which occur in the liquid phase and on the solid surface. These industries include biological engineering, nanofluidics, and catalysis.
- **Closing research gap**: The combined effects of convective heating, thermal radiation, dissipated heat from porous media, H-H chemical reaction, and mixed convections flow of the Papanastasiou model in the context of stretchable sheets have received little consideration, despite the fact that researchers have employed LM-ANN to analyze HNF dynamics. Closing this knowledge gap is my motivation for this study.

1.2. Novelty of the model

The novel aspects of the study are given below:

- In this study, I investigate the Darcy-Forchheimer boundary layer flow of a Papanastasiou-Bingham viscoplastic hybrid NF over a convectively heated stretched surface inserted into a porous medium. The Forchheimer inertia dissipation term is integrated directly into the energy equation to physically represent frictional heating in the porous matrix. The shape-specific CNT and Al_2O_3 nanoparticles are dispersed in dihydrogen as a base fluid. The viscoplastic NF framework is expanded beyond the traditional single-buoyancy formulations documented in the literature by the simultaneous coupling of H-H cubic autocatalytic chemical reactions with thermal and dual-solutal mixed convection buoyancy forces, arising independently from each reaction type through distinct solutal Grashof numbers.
- An investigation of dihydrogen-based Papanastasiou HNF flow containing Al_2O_3 and CNT of various shaped (spherical and platelet-shaped) nanoparticles at constant temperature 35°C [34] is conducted.
- The mixed convection due to temperature difference and H-H reaction effects due to chemical species $\mathcal{A}$ and $\mathcal{B}$ are considered for the first time.

- An examination of how the system is affected by various model parameters that modify the statistical data in the LM-ANN method is conducted. By contrasting the results to the data available, the accuracy of the procedure is confirmed, and minimum relative errors are revealed.
- The radiative NF Darcy-Forchheimer flow over a stretching sheet and the nanofluidics problem have been resolved by investigators using numerical methods. However, the LM-ANN approach has not been applied to water-based Papanastasiou HNF flow containing Al_2O_3 and CNT of various shaped (spherical and platelet-shaped) nanoparticles at constant temperature and volume frictions of 5% and 0% with a H-H chemical reaction and convective boundary conditions. This new method of an AI-based solution is thus used to perform a comprehensive analysis of the complicated fluid dynamics problem.

The paper is organized in the following manner: In Section 2, I provide problem formulations based on assumptions and BL approximations. In Section 3, I provide the results and discussion. In Section 4, I conclude the paper.

2. Problem formulations

Consider the Darcy-Forchheimer, radiative, incompressible, and mixed convection flow of Papanastasiou-Bingham HNF comprising two nanomaterials (CNT and Al_2O_3) over a stretching sheet submerged in a porous media following the Darcy-Forchheimer relation. The location of the sheet is along a horizontal $x-$direction, while the confinement of the fluid is in the $y-$direction. Furthermore, more practical assumptions of the problem are taken to formulate the problem:

- The fluid achieves a comparable velocity profile at the boundary as a result of the elastic sheet horizontal stretching with an elastic strain rate in the $x-$direction, which is enforced by the no-slip requirement.
- The momentum equation of Papanastasiou-Bingham HNF incorporates the mixed convection and Darcy-Forchheimer feature.
- A is distributed throughout the fluid, but it is depleted near the stretching surface by the heterogeneous reaction.
- I use dihydrogen as the basis fluid and examine the nanomaterial CNTs in a spherical form and alumina in a platelet shape [35]. Further explanation of the flow model is given in Figure 1. The body force contributing to the momentum equation is the mixed convection and Darcy-Forchheimer relation [36].
- Analysis of the convective boundary condition for heat transfer is carried out. Mixed convection effects are also taken into consideration during autocatalysis cubic chemical reactions.
- Furthermore, assumptions such as wall velocity $u_w = ax$, fluid temperature $\bar{T}$, and ambient temperature $\bar{T}_\infty$ are taken.

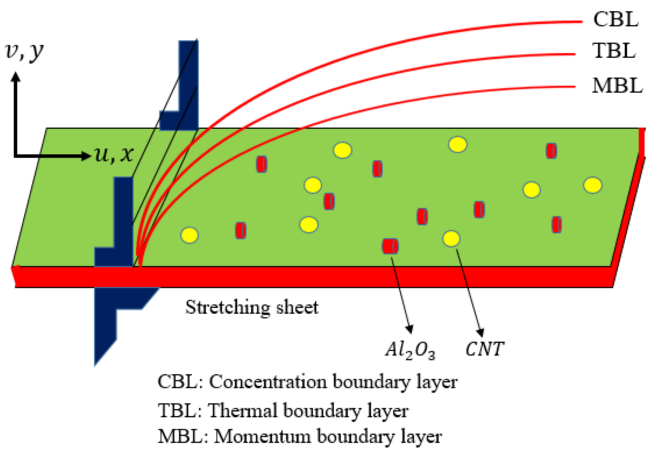

Figure 1. Illustration of the governing problem.

The constitutive equations comprising the Darcy-Forchheimer dissipative flow of Papanastasiou-Bingham HNF are defined as [37–39]:

$$\frac{\partial \bar{u}}{\partial x} + \frac{\partial \bar{v}}{\partial y} = 0, \tag{7}$$

$$\rho_{Hnf}\left(\bar{u}\frac{\partial \bar{u}}{\partial x} + \bar{v}\frac{\partial \bar{u}}{\partial y}\right) = \frac{\partial \tau_{xx}}{\partial y} + \frac{\partial \tau_{xy}}{\partial y}, \tag{8}$$

$$\rho_{Hnf}\left(\bar{u}\frac{\partial \bar{v}}{\partial x} + \bar{v}\frac{\partial \bar{v}}{\partial y}\right) = \frac{\partial \tau_{xy}}{\partial y} + \frac{\partial \tau_{yy}}{\partial y}. \tag{9}$$

$$\left(\rho c_p\right)_{Hnf}\left(\bar{u}\frac{\partial \bar{T}}{\partial x} + \bar{v}\frac{\partial \bar{T}}{\partial y}\right) = k_{Hnf}\left(\frac{\partial^2 \bar{T}}{\partial x^2} + \frac{\partial^2 \bar{T}}{\partial y^2}\right) - \frac{16\sigma^* \bar{T}_\infty^3}{3\kappa^*}\left(\frac{\partial^2 \bar{T}}{\partial x^2} + \frac{\partial^2 \bar{T}}{\partial y^2}\right) + \Phi_{Visc} + \Phi_{Darcy} + \Phi_F. \tag{10}$$

Here, Φ_{Visc}, Φ_{Darcy}, and Φ_F are the viscous dissipation term due to viscosity, Darcy, and the Forchheimer term, respectively.

Mathematically,

$$\Phi_{Visc} = \mu_{app} \cdot \left(\frac{\partial u}{\partial y}\right)^2,\ \Phi_{Darcy} = \frac{\mu_{app}}{K^*}\bar{u}^2,\ \Phi_F = \frac{\rho_{Hnf} C_d}{\sqrt{K^*}}\bar{u}^3. \tag{11}$$

Using

$$\tau_{xx} = \left(\mu_{Hnf} + \frac{\hat{\tau}_0}{\frac{\partial \bar{u}}{\partial x}}\left(1 - e^{-n\frac{\partial \bar{u}}{\partial x}}\right)\right),\ \tau_{xy} = \left(\mu_{Hnf} + \frac{\hat{\tau}_0}{\frac{\partial \bar{u}}{\partial y}}\left(1 - e^{-n\frac{\partial \bar{u}}{\partial y}}\right)\right),\ \tau_{yx} = \left(\mu_{Hnf} + \frac{\hat{\tau}_0}{\frac{\partial \bar{u}}{\partial x}}\left(1 - e^{-n\frac{\partial \bar{u}}{\partial x}}\right)\right),\ \tau_{yy} = \left(\mu_{Hnf} + \frac{\hat{\tau}_0}{\frac{\partial \bar{v}}{\partial x}}\left(1 - e^{-n\frac{\partial \bar{v}}{\partial x}}\right)\right). \tag{12}$$

Using BL approximations $\bar{u} \gg \bar{v}$, $\frac{\partial \bar{u}}{\partial y} \gg \frac{\partial \bar{u}}{\partial x}$ the governing equations takes the following form [40,41]:

$$\frac{\partial \bar{u}}{\partial x}+\frac{\partial \bar{v}}{\partial y}=0, \tag{13}$$

$$\rho_{Hnf}\left(\bar{u}\frac{\partial \bar{u}}{\partial x}+\bar{v}\frac{\partial \bar{u}}{\partial y}\right)=\frac{\partial}{\partial y}\left(\left(\mu_{Hnf}+\frac{\hat{\tau}_0}{\frac{\partial \bar{u}}{\partial y}}\left(1-e^{-n\frac{\partial \bar{u}}{\partial y}}\right)\right)\frac{\partial \bar{u}}{\partial y}\right)-\frac{1}{K^*}\left(\mu_{Hnf}+\frac{\hat{\tau}_0}{\frac{\partial \bar{u}}{\partial y}}\left(1-e^{-n\frac{\partial \bar{u}}{\partial y}}\right)\right)\bar{u}-$$

$$\frac{\rho_{Hnf}C_d}{\sqrt{K^*}}\bar{u}^2+g\{\delta_T(\bar{T}-\bar{T}_\infty)+\delta_{\bar{C}_1}(\bar{C}_1-\bar{C}_{1_\infty})+\delta_{\bar{C}_2}(\bar{C}_2-\bar{C}_{2_\infty})\}, \tag{14}$$

$$(\rho c_p)_{Hnf}\left(\bar{u}\frac{\partial \bar{T}}{\partial x}+\bar{v}\frac{\partial \bar{T}}{\partial y}\right)=\left(k_{Hnf}+\frac{16\sigma^*\bar{T}_\infty^3}{3\kappa^*}\right)\frac{\partial^2 \bar{T}}{\partial y^2}+\left(\mu_{Hnf}+\frac{\hat{\tau}_0}{\frac{\partial \bar{u}}{\partial y}}\left(1-e^{-n\frac{\partial \bar{u}}{\partial y}}\right)\right)\left(\frac{\partial u}{\partial y}\right)^2+\frac{1}{K^*}\left(\mu_{Hnf}+\right.$$

$$\left.\frac{\hat{\tau}_0}{\frac{\partial \bar{u}}{\partial y}}\left(1-e^{-n\frac{\partial \bar{u}}{\partial y}}\right)\right)\bar{u}^2+\frac{\rho_{Hnf}C_d}{\sqrt{K^*}}\bar{u}^3, \tag{15}$$

$$\left(\bar{u}\frac{\partial \bar{C}_1}{\partial x}+\bar{v}\frac{\partial \bar{C}_1}{\partial y}\right)=D_{\mathcal{A}}\frac{\partial^2 \bar{C}_1}{\partial y^2}-\bar{k}_1\bar{a}\bar{b}, \tag{16}$$

$$\left(\bar{u}\frac{\partial \bar{C}_2}{\partial x}+\bar{v}\frac{\partial \bar{C}_2}{\partial y}\right)=D_{\mathcal{B}}\frac{\partial^2 \bar{C}_2}{\partial y^2}+\bar{k}_1\bar{a}\bar{b}. \tag{17}$$

With the surface $y \to 0$ and free surface $y \to \infty$ conditions [42,43]:

$$u=u_w=ax, v=0, D_{\mathcal{A}}\frac{\partial \bar{C}_1}{\partial y}=\bar{k}_2\bar{a},\ D_{\mathcal{B}}\frac{\partial \bar{C}_2}{\partial y}=-\bar{k}_2\bar{a}, -k_{Hnf}\frac{\partial \bar{T}}{\partial y}=H_F(\bar{T}-\bar{T}_w), \tag{18}$$

$$\bar{T}\to\bar{T}_\infty, \bar{C}_1\to\bar{C}_0, \bar{C}_2\to 0,\ u\to 0. \tag{19}$$

In the above expression/equations, $\bar{u}$ and $\bar{v}$ are the components of velocity, C_d is the Forchheimer coefficient, K^* is the medium porosity, p correspond to pressure, $D_{\mathcal{B}}$, and $D_{\mathcal{A}}$ are the, heat capacity, nanomaterial heat capacitance, and diffusion species of $\mathcal{B}$ and $\mathcal{A}$. Furthermore, H_F, δ_T, δ_C, and g are the coefficients of heat transfer, thermal, concentration expansion, and gravitational acceleration, respectively. For diluted diffused nanoparticle suspensions at moderate volume fractions ($\varphi \leq 5\%$), the Brinkman and Maxwell-Bruggeman correlations used for the effective viscosity and thermal conductivity of the CNT–Al_2O_3 hybrid NF are well-validated. They have also been thoroughly benchmarked against experimental data for oxide and carbon-based nanoparticle systems. Adoption of more sophisticated models that incorporate nanoparticle aggregation, cross-facial thermal resistance, and temperature-dependent property variations could significantly refine the predicted heat transfer and skin friction results without changing the qualitative physical trends reported in this study, even though these correlations offer physically consistent estimates within the current operating range. The volumetric friction of Al_2O_3 is denoted by $\varphi_{Al_2O_3}$, and CNTs by φ_{CNT}. Thus, the total volume friction of both nanomaterials is $\varphi = \varphi_{Al_2O_3}+\varphi_{\mathrm{CNT}}$. Details of the expression for HNF density, thermal conductivity, thermal expansion, and heat capacitance are (ρ_{Hnf}), $(\rho\delta_T)_{Hnf}$, k_{Hnf}, and $(\rho c_p)_{Hnf}$, respectively. The mathematical representation for cylindrical and platelet nanomaterials are [35,44]:

$$\rho_{Hnf} = 1 - \left(\varphi_{Al_2O_3} + \varphi_{\mathrm{CNT}}\right)\rho_{bf} + \varphi_{Al_2O_3}\rho_{Al_2O_3} + \varphi_{\mathrm{CNT}}\rho_{\mathrm{CNTs}}, \tag{20}$$

$$(\rho\delta_T)_{Hnf} = 1 - \left(\varphi_{Al_2O_3} + \varphi_{\mathrm{CNT}}\right)(\rho\delta_T)_{bf} + \varphi_{Al_2O_3}(\rho\delta_T)_{Al_2O_3} + \varphi_{\mathrm{CNT}}(\rho\delta_T)_{\mathrm{CNTs}}. \tag{21}$$

The expression for $\left(\rho c_p\right)_{Hnf}$ for cylindrical and platelet nanomaterials is [35]:

$$\left(\rho c_p\right)_{Hnf} = 1 - \left(\varphi_{Al_2O_3} + \varphi_{\mathrm{CNT}}\right)\left(\rho c_p\right)_{bf} + \varphi_{Al_2O_3}\left(\rho c_p\right)_{Al_2O_3} + \varphi_{\mathrm{CNT}}\left(\rho c_p\right)_{\mathrm{CNTs}}. \tag{22}$$

Several estimates for μ_{Hnf} and k_{Hnf} spherical and platelet nanomaterials are investigated in this study. This is required for a feasible model since the density of nanomaterials is influenced by their physical shape. The viscosity and thermal conductivity of the NF produced by higher-density nanoparticles might differ [34].

$$\mu_{Hnf} = \frac{\left(\varphi_{Al_2O_3}\mu_{nfAl_2O_3} + \varphi_{\mathrm{CNT}}\mu_{nf\mathrm{CNT}}\right)}{\varphi}, \tag{23}$$

$$k_{Hnf} = \frac{\left(\varphi_{Al_2O_3}k_{nfAl_2O_3} + \varphi_{\mathrm{CNT}}k_{nf\mathrm{CNT}}\right)}{\varphi}. \tag{24}$$

Here, μ_{Hnf} and k_{Hnf} for spherical and platelet nanomaterials are defined as [35]:

$$\mu_{nfAl_2O_3} = \left(6.2\varphi_{Al_2O_3}^2 + 2.5\varphi_{Al_2O_3} + 1\right)\mu_{bf},\ k_{nfAl_2O_3} = k_{bf}\left(\frac{-2\varphi_{Al_2O_3}\left(k_{bf} - k_{Al_2O_3}\right) + 2k_{bf} + k_{Al_2O_3}}{\varphi_{Al_2O_3}\left(k_{bf} - k_{Al_2O_3}\right) + 2k_{bf} + k_{Al_2O_3}}\right), \tag{25}$$

$$k_{nf\mathrm{CNT}} = \left(612.6\varphi_{\mathrm{CNT}}^2 + 37.1\varphi_{\mathrm{CNT}} + 1\right)\mu_{bf},\ k_{nf\mathrm{CNT}} = k_{bf}\left(\frac{-4.7\varphi_{A\mathrm{CNT}}\left(k_{bf} - k_{\mathrm{CNT}}\right) + 4.7k_{bf} + k_{\mathrm{CNT}}}{\varphi_{\mathrm{CNT}}\left(k_{bf} - k_{\mathrm{CNT}}\right) + 2k_{bf} + k_{\mathrm{CNT}}}\right). \tag{26}$$

The physical configuration and chemical characteristics of nanomaterials and water are displayed in Table 1.

Table 1. Physical configuration and chemical characteristics of nanomaterials and water [45–47].

	Nanomaterial shape	Shape factor	$\rho: (Kgm^{-3})$	$k: (Wm^{-1}K^{-1})$	$c_p: (Jk^{-1}g^{-1}K^{-1})$	$\delta_T(K^{-1})$
$\varphi_{Al_2O_3}$	Platelet	5.7	3970	40	765	0.85
φ_{CNT}	Spherical	3.0	2100	3007.4	410	44
Water			997.1	0.6130	4179	21

Employing similarity variables [48–50]:

$$\psi = x\sqrt{v_f}f(\eta),\ \eta = y\sqrt{\frac{c}{v_f}},\ \Theta(\eta) = \frac{T-T_\infty}{T_w-T_\infty},\ G(\eta) = \frac{\bar{a}}{\bar{a}_\infty},\ H(\eta) = \frac{\bar{b}}{\bar{a}_\infty}. \tag{27}$$

The component velocity (u, v) is:

$$u = cxf'(\eta),\ v = -\sqrt{cv_f}f(\eta). \tag{28}$$

The governing dimensionless equations takes the following form:

$$f'''\left(1 + n^*Bn\left(e^{-n^*\sqrt{Re}f''}\right)\right) + \frac{n_2}{n_1}(ff'' - f'^2) - \frac{n_2}{n_1}D_a\left(1 + \frac{Bn}{\sqrt{Re}f''}\left(1 - e^{-n^*\sqrt{Re}f''}\right)\right)f' - F_r f'^2 + \frac{n_3}{n_1}\lambda_m(\Theta - \gamma_1 G - \gamma_2 H) = 0, \tag{29}$$

$$\left(n_5 + \frac{4}{3}Nr\right)\Theta'' + n_4 Pr(f'\Theta - f\Theta') + n_2 n_4 PrEc\left(1 + \frac{Bn}{\sqrt{Re}f''}\left(1 - e^{-n^*\sqrt{Re}f''}\right)(f''^2 + D_a f'^2)\right) + n_2 n_4 PrEcF_r f'^3 = 0, \tag{30}$$

$$G'' + ScfG' - ScK_r GH^2 = 0, \tag{31}$$

$$\beta H'' + ScfH' + ScK_r GH^2 = 0. \tag{32}$$

With

$$f'(0) = 1, f(0) = 1, \Theta(0) = 1,\ G'(0) = K_S G(0),\ \beta H'(0) = -K_S G(0), \tag{33}$$

$$f'(\infty) \to 0,\ \Theta(\infty) = 0,\ G(\infty) \to 1,\ H(\infty) \to 0. \tag{34}$$

It is assumed that $\mathcal{B} = \mathcal{A}$, which gives $D_{\mathcal{B}} = D_{\mathcal{A}}$, with $\beta = 1$.

$$G(\eta) + H(\eta) = 1. \tag{35}$$

Using Eq (29), Eq (26) takes the following form:

$$G'' + ScfG' - ScK_r G(1 - G^2) = 0. \tag{36}$$

Additionally,

$$G'(0) = K_S G(0),\ G(\infty) \to 1. \tag{37}$$

Associated parameters/numbers with dimensionless equations are shown in Table 2.

Table 2. Associated parameters/numbers with dimensionless equations.

Symbolic representation	Name	Range/ default values
$Bn = \frac{\tau_y^*}{\mu_f c}$	Bingham number	[0, 10] source [51]
$n^* = cn$	Growth parameter	[0, 1000s] source [52]
$Re_x = \frac{ax^2}{v_f}$	Reynold number	[0, 1000] source [53]
$D_a = \frac{v_f}{aK^*}$	Darcy number	[0, 1] source [54]
$F_r = \frac{C_d}{\sqrt{K^*}}$	Forchheimer parameter	[0, 3] source [54]
$Pr = \frac{\mu_f c_p}{k_f}$	Prandtl number	6.2 source [55]
$Ec = \frac{(u_w)^2}{c_p(T_w - T_\infty)}$	Eckert number	[0, 1] source [55]
$Nr = \frac{4\sigma^* \bar{T}_\infty^3}{\kappa^* k_f}$	Radiative parameter	[0, 1] source [55]
$Sc = \frac{v_f}{D_B}$	Schmidt number	[0, 3] source [46]
$K_r = \frac{\bar{k}_1 \bar{a}_\infty^2}{c}$	Homogenous reaction rate parameter	[0, 3] source [56]
$K_S = \frac{\bar{k}_2}{D_A}\sqrt{\frac{c}{v_f}}$	Heterogeneous reaction rate parameter	[0, 1] source [56]
$\beta = \frac{D_B}{D_A}$	Diffusion ratio coefficient	[0, 1] source [56]
$\lambda_m = \frac{Gr_T}{Re_x^2}$	Mixed convection parameter	[0, 5] source [56]
$Gr_T = \frac{u_w \delta_T (\bar{T} - \bar{T}_\infty) g}{v_f^2}$	Thermal Grashof number	[0, 1] source [46]
$\gamma_1 = \frac{u_w \delta_{\bar{C}_1} (\bar{C}_1 - \bar{C}_{1\infty})) g}{v_f^2}$	Solutal Grashof number due to Homogenous reaction	Default value [0, 1]
$\gamma_2 = \frac{u_w \delta_{\bar{C}_2} (\bar{C}_2 - \bar{C}_{2\infty})) g}{v_f^2}$	Solutal Grashof number due to Heterogeneous reaction	Default value [0, 1]

2.1. Physical quantities

Dimensionless metrics such as skin friction C_f, Nusselt number Nu_x, and Sherwood number Sh_x are employed to characterize many physical processes in fluid dynamics and transport phenomena. A fluid shear stress or drag force as it passes over a solid surface is referred to as skin friction. Especially in streamlined shapes, this surface friction contributes significantly to total drag. The improvement in heat transfer by convection over conduction alone is measured by Nu_x, a dimensionless ratio in heat transfer. Heat transfer via convection is more prevalent, when Nu_x is larger. Last, the mass transfer is quantified by the Sherwood number Sh_x. A higher Sh_x indicates that fluid motion, not molecular diffusion, is the primary force behind the transfer of a chemical species. It is a measure of the ratio of convective transfer of mass to diffusive mass transfer. Mathematically, these quantities are described as:

$$\tau_w^* = \left(\mu_f + \frac{\tau_y^*}{\frac{\partial \bar{u}}{\partial y}}\left(1 - e^{-n\frac{\partial \bar{u}}{\partial y}}\right)\right)\frac{\partial \bar{u}}{\partial y}\bigg|_{y=0}, \quad q_w = \left(-k_f \frac{\partial \bar{T}}{\partial y} + q_r\right)\Big|_{y=0}, \quad q_m = -D_{\mathcal{A}}\left(\frac{\partial \bar{C}_1}{\partial y}\right)\Big|_{y=0}, \tag{38}$$

$$Re_x^{\frac{1}{2}} C_f = \frac{1}{n_1}\left(f''(0) + \frac{Bn}{\sqrt{Re}f''}\left(1 - e^{-n^*\sqrt{Re}f''(0)}\right)\right), Re_x^{-\frac{1}{2}} Nu_x = -\left(n_5 + \frac{4}{3}Nr\right)\Theta'(0), \; Re_x^{-\frac{1}{2}} Sh_x = -G'(0). \tag{39}$$

2.2. Methodology framework

2.2.1. Data generation implementing the numerical RKF45 technique

In this study, I use a computational integration technique called "Runge–Kutta–Fehlberg fourth-fifth order (RKF45)" that invokes the shooting procedure [57] to solve the nonlinear ordinary differential equations (ODEs), Eqs (17), (18), and (23), with the suitable set of boundary conditions stated in Eqs (20), (21), and (24). Using incorporated error prediction to dynamically modify step size, such as larger steps in smooth regions and smaller steps where solutions fluctuate quickly, offers high accuracy with automatic error control. This balances computational cost with precision, making it more reliable and efficient than fixed-step approaches. It is not strictly symmetrical (bad for long-term Hamiltonian systems), requires impractically small steps, and is more computationally expensive per step than lower-order approaches. It can also have trouble with stiff equations. Additionally, error estimates may fail close to singularities or discontinuities. The governed problem and boundary conditions are first converted to a system of first-order equations using this procedure. The technique maintains the local truncation error below a user-defined absolute/relative error tolerance by varying the step size. Accuracy is increased with tighter tolerance, but steps and runtime are increased. If the calculated error is within tolerance, the step is allowed; if not, it is rejected, and a smaller step is attempted. The ratio tolerance 10^{-6} is used to update the step size, guaranteeing that the local error is driven toward zero, while the global error stays constrained, and the solution converges within the given accuracy. The relevant initial strategies (zeroth order) are then selected, and they have to confirm the boundary conditions under consideration [58]. The shooting procedure is repeated so that there are no numerical oscillations in order to meet the convergence threshold of 10^{-6}. The choice of $\eta \to \infty$ or η_∞ ranges from 0 to 5, and the step-size $\Delta\eta = 0.001$ is used. The results of model are validated for $f'(\eta)$ and $\Theta(\eta)$, by assuming $Bn = 0,\ \lambda_m = 0,\ Da = 0, Fr = 0,\ Nr = 0$, and $\varphi = 0$.

2.2.2. Employment of ANNs

A vital aspect of contemporary machine learning is ANNs, which use networked computing units to deal with input concurrently. They are used in a wide range of domains, including computational modeling, identification of patterns, regression analysis, computational biology, system administration, and time-series analysis. The LM algorithm enhances the ANNs functionality by ensuring computational stability and fast growth, especially in complex fluid mechanics problems, demonstrating the adaptability and value of ANNs. In ths fluid flow model, ANNs with various architectures are used to incorporate ODEs. When implementing LM-ANNs, the following crucial operational steps are frequently taken:

- The LM-ANN methodology begins by identifying the critical factors that require simulation.
- An output-input pair data is generated using the RK45 solver, with the flow-directing factors identified in the first phase serving as the inputs.
- This data set is then subjected to training, typically with subgroups for validation and training.
- The effectiveness of the ANNs is assessed using metrics such as mean squared error (MSE), R^2, and root mean square error (RMSE).
- Tuning the parameters for training is necessary to increase the algorithm's precision and overall accuracy. If the model cannot achieve the desired degree of precision, steps 2 to 5 are repeated in an iterative manner to enhance the process.

I implement the LM Algorithm together with ANNs by analyzing numerical results obtained from the altered model description using the RK45 methodology. Three subsets of the assembled datasets are chosen at random, with 80% for training and 10% for validation and testing. I use 800 data samples in all, of which 120 are utilized for validation and testing and 680 are used for training. Moreover, I focus on case studies with five situations and three cases each that employ the LM-ANNs methodology. The standard dataset is produced for the temperature, concentration, and velocity profiles for an input level of 0 to 6 with an interval step of a single unit. Table 3 gives a summary of the fundamental structure of the LM-ANN, while a review of the ANN settings criteria for variables is given in Table 4. An activation function tangent sigmoid (Tan-Sig) is used by the hidden layer nodes of the ANN model, whereas a Purelin (linear) activation function is implemented by the output layer. The resulting layer of ANN model uses the purelin function as its activation function, and the Tan-Sigmoid function [62] for the transfer function in the hidden layer.

$$f(\bar{x}) = \frac{1}{1+e^{-(\bar{x})}},\ purelin(\bar{x}) = \bar{x}. \tag{40}$$

The forecasting accuracy and operational efficiency of the ANN model must be evaluated after it has been designed. The MSEs are calculated to assess the model’s efficacy.

$$\text{MSE}= \frac{1}{n}\left(\sum_{j=1}^{n}\left(\mathbb{X}_{actual(j)} - \mathbb{X}_{predicted(j)}\right)^2\right), \tag{41}$$

The detail of R^2 is calculated using the following formula:

$$R = \sqrt{1 - \frac{\sum_{j=1}^{n}\left(\mathbb{X}_{actual(j)} - \mathbb{X}_{predicted(j)}\right)^2}{\sum_{j=1}^{n}\mathbb{X}_{actual(j)}}}. \tag{42}$$

The RMSE formula is defined as:

$$\text{RMSE}= \sqrt{\frac{1}{n}\left(\sum_{j=1}^{n}\left(\mathbb{X}_{actual(j)} - \mathbb{X}_{predicted(j)}\right)^2\right)}. \tag{43}$$

The relative error of ANN is further estimated by % error,

$$\% \text{ Error}=\frac{(\mathbb{X}_{actual(j)}-\mathbb{X}_{predicted(j)})}{\mathbb{X}_{actual(j)}}\times 100. \tag{44}$$

Here, $\mathbb{X}_{actual(j)}$ and $\mathbb{X}_{predicted(j)}$ are the actual and predicted values of ANN. The LMB-ANN is independently reconfigured 20 times for each profile using distinct random seeds that control dataset segmentation and weight initialization to evaluate statistical repeatability. According to Table 4, the mean MSE stays below 3.9×10^{-12} with a standard deviation below 5.4×10^{-11}, and the mean R^2 stays above 0.999995 with a standard deviation below 6×10^{-10} across all three profiles. The reported best-case metrics (MSE = 2.5188×10^{-12}, R^2 =0.999999) are statistically valid of the typical training outcome and are not the result of a single favorable initialization, as confirmed by these minuscule variability measures. The high reproducibility can be attributed to the second-order convergence features of the L-M algorithm. Table 5 shows the specifications and configurations of the suggested LMB-ANN design. The Neuron structure of the ANN is provided in Figure 2, while details of the methodology are depicted in Figure 3.

Table 3. Validation check for Nu_x with prior studies.

Pr	Ishak [59]		Jamshed et al. [60]		Present	
0.72	0.8086		0.8087618		0.8087612	
1.00	1.0000		1.0000000		1.0000000	
3.00	1.9236		1.9235742		1.9235747	
7.00	3.0723		3.0731465		3.0731469	
10.0	3.7006		3.7205542		3.0731468	
Pr	Ref. [61]		Ref. [46]		Present results	
	$f'(\eta)$	$\Theta(\eta)$	$f'(\eta)$	$\Theta(\eta)$	$f'(\eta)$	$\Theta(\eta)$
0.00	0.00000	0.10732	0.000000	0.107320	0.00000	0.10731
0.30	0.40830	0.04938	0.408300	0.049380	0.40830	0.04937
0.50	0.65606	0.65605	0.656061	0.656061	0.65605	0.65605
0.70	0.85538	0.85538	0.855383	0.855383	0.85537	0.85537
1.00	0.00000	0.00000	0.000000	0.000000	0.00000	0.00000

Table 4. Statistical reproducibility across 20 independent runs.

Profile	Mean R^2	Mean MSE	Min-Max R^2
$f'(\eta)$	0.999997	2.674×10^{-10}	0.999991-0.999999
$\Theta(\eta)$	0.999996	3.148×10^{-10}	0.999989-0.999999
$G(\eta)$	0.999995	3.892×10^{-10}	0.999986-0.999999

Table 5. The specifications and configurations of the suggested LMB-ANN design.

Catalogue	Elucidation
Learning method	LM
Overall samples	800
Training data in %	80
Validation data in %	10
Testing data in %	10
Hidden deposits	10 to 20 layers
Produced dataset	RK45 methodology
MSE values (Fitness)	0
Sample assortment	Random
Extreme epochs	1000
Stopping criterion	Default

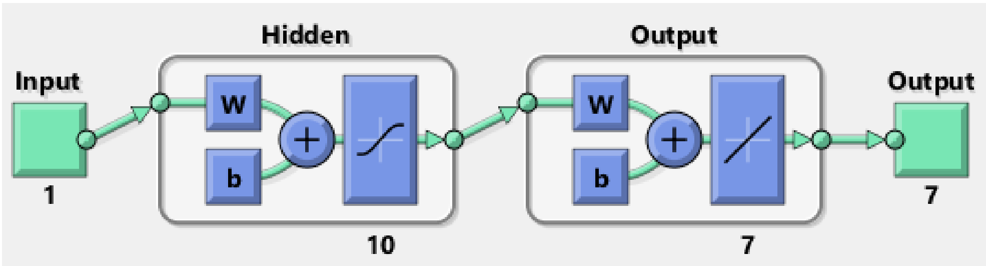

Figure 2. Neuron structure of ANN.

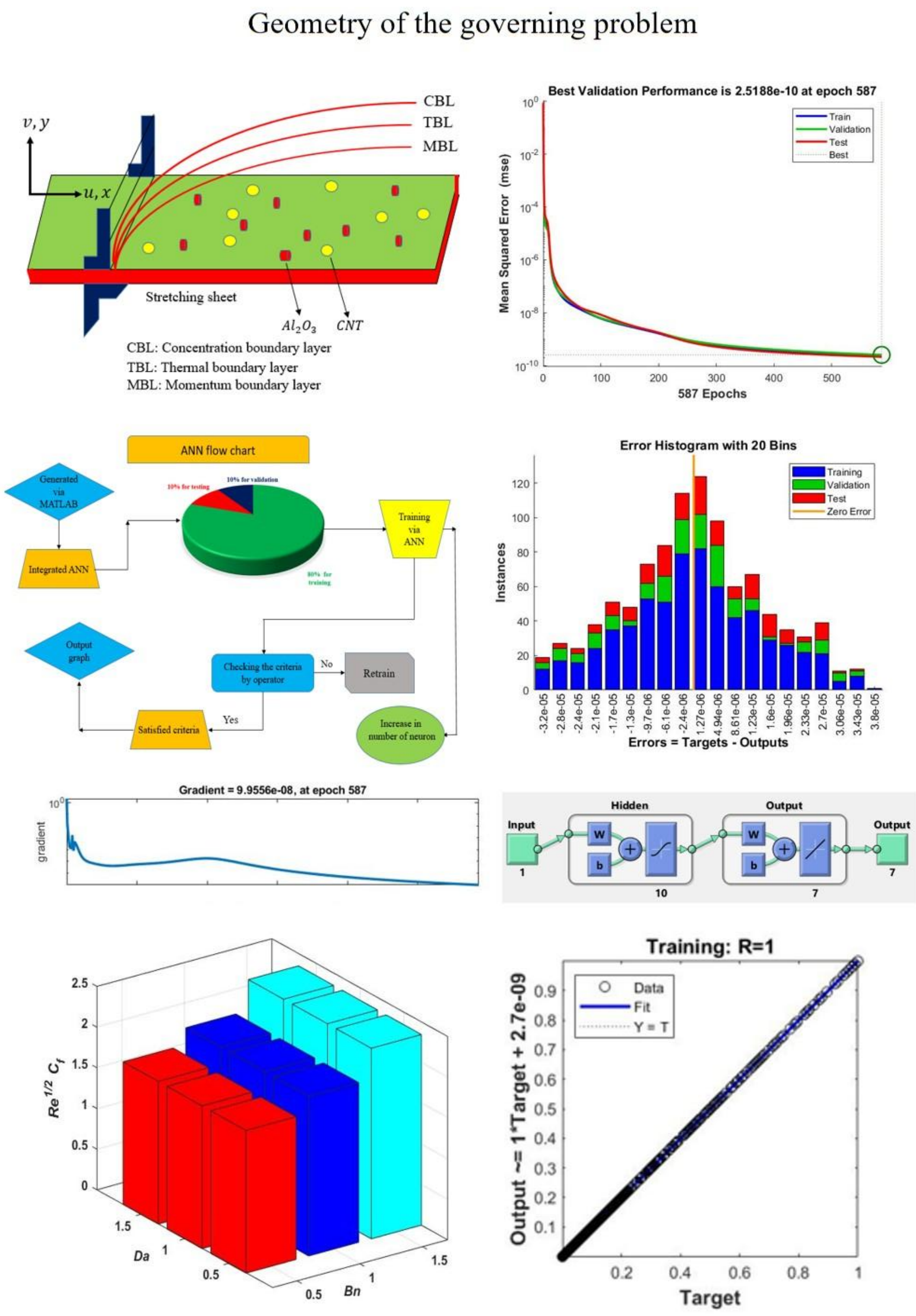

Figure 3. Methodology detail of the problem.

3. Results and discussion

The Darcy-Forchheimer dissipative flow of the Papanastasiou-Bingham HNF model results are assessed using artificial-numerical computing and within the suggested LMAANN framework, which is specified in Eqs (17), (18), and (23). Table 4 highlights the different cases (C1, C2, C3) for three Papanastasiou-Bingham HNF model different profile ($f'(\eta)$, $\Theta(\eta)$, and $G(\eta)$) scenarios examined in this work. Among the 800 entries, 80% are used for training, 10% for testing, and 10% for validation. The neural network is generated using the MATLAB "nftool" function and features a single concealed layer with ten neurons. The LM algorithm uses the nftool default trained approach to lower prediction errors. The Purelin activation functions are used in the output layer, while tang-sigmoid activation functions are used in the hidden layer. For training, an objective of 10^{-6} is established, which may go on for up to 1000 epochs. By assessing the correctness of the Papanastasiou-Bingham HNF model using MSE, the training state, error histogram (EH), and regression plots, a strong validation is possible. Tables 6–9 describe a variety of scenarios that center on changing the model parameters. Each table presents examples with distinct parameter values showing how the model time operation, number of epochs, mu, gradient index, and MSE are changed. Together, these scenarios offer a thorough understanding of how each parameter influences the model's reliability and stability in various testing settings.

Table 6. Detail of governing parameters, scenario, and cases.

Profiles	Cases	Model parameters				
		γ_1	γ_2	Bn	λ_m	Nr
$f'(\eta)$ (S1)	C1	0.1	0.1	0.1	0.1	0.1
	C2	0.6	0.6	0.6	0.6	0.6
	C3	1.1	1.1	1.1	1.1	1.1
$\Theta(\eta)$ (S2)	C1	0.1	0.1	0.1	0.1	0.1
	C2	0.6	0.6	0.6	0.6	0.6
	C3	1.1	1.1	1.1	1.1	1.1
$\mathrm{G}(\eta)$ (S3)	C1	0.1	0.1	0.1	0.1	0.1
	C2	0.6	0.6	0.6	0.6	0.6
	C3	1.1	1.1	1.1	1.1	1.1

Table 7. Performance metrics of LM-ANN for $f'(\eta)$.

Measures/ value	Epoch	Performance	Gradient	Mu	Validation Checks	Time
Start at	0	3.35	4.63	0.0001	0	−
Stopped at	587	2.5188×10^{-10}	9.95×10^{-9}	1×10^{-9}	0	0.00.01
Target	1000	0	10^{-8}	10^{-10}	6	−

Table 8. Performance metrics of LM-ANN for $\Theta(\eta)$.

Measures/ value	Epoch	Performance	Gradient	Mu	Validation Checks	Time
Start at	0	3.87	4.02	0.0001	0	–
Stopped at	577	1.3039×10^{-9}	9.96×10^{-8}	1×10^{-9}	0	0.00.02
Target	1000	0	10^{-9}	10^{-10}	6	–

Table 9. Performance metrics of LM-ANN for $G(\eta)$.

Measures	Epoch	Performance	Gradient	Mu	Validation Checks	Time
Start at	0	5.18	1.92	0.0001	0	–
Stopped at	781	7.0351×10^{-10}	9.99×10^{-8}	1×10^{-8}	0	0.00.03
Target	1000	0	10^{-9}	10^{-10}	6	–

The findings for the three anticipated scenarios pertaining to the proposed Papanastasiou-Bingham HNF model using the LM-ANN technique are shown in Figures 4–6. Figure 4(a–d) shows the MSE values, gradient performance, control parameter mu, and EH of Bingham parameter for velocity profile. The MSE epoch scores, which display the network performance at different intervals, are significant. The recorded MSE for scenario S1 is 2.5188×10^{-10} at a 587 epoch, is shown in Figure 4(a). Better performance is indicated by lower MSEs, which is 2.5188×10^{-10}. The learning accuracy of the network is indicated by these plots. The complexity and non-linearity of the simulated situations are highlighted by the range in epochs required to achieve these MSEs, showing how different situations require different levels of training for optimal outcomes. Figure 4(b) shows the convergence performance, coherence, and predictability of case 3 simulation maintenance inside the architecture. Parameter Mu, which represents the gradients and step size, is an important consideration in this case. For S1, the value of Mu is set to 1×10^{-9} at a 587 epoch. The gradient values for scenario S1 is 9.95×10^{-8}. A notable pattern of decreasing Mu and gradient values over time is depicted in the graph, suggesting stability and convergence as well as the need for less network reconfiguration as it develops. This decrease demonstrates that the changes become less frequent and smaller as the network approaches peak performance. Additionally, it is associated with increased testing and training efficiency. Figure 4(c), which incorporates EH, provides a comprehensive behavioral assessment of errors. The error bar is a very helpful tool that illustrates the distribution of errors throughout the training process. As can be seen from the case 3 histogram, most errors are positive throughout scenarios, with the erroneous box of references mainly located above the zero axes. The regression plots presented in Figure 4(d) further confirm the model dependability. The regression coefficient of determination R^2 is equal to one when there is an ideal link between the predicted and real information obtained. Because each target point lands precisely on the regression line, the model's predicted dependability is demonstrated. The absolute errors, demonstrated by all the figures, ranges from 10^{-8} to 10^{-5}. These results provide more evidence that the Papanastasiou-Bingham HNF model is reliable.

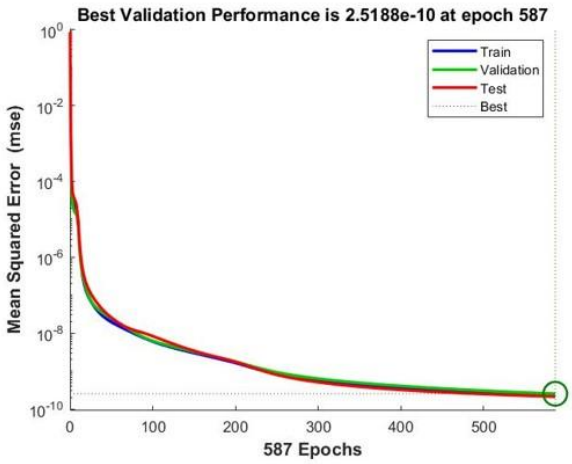

(a) Performance plot.

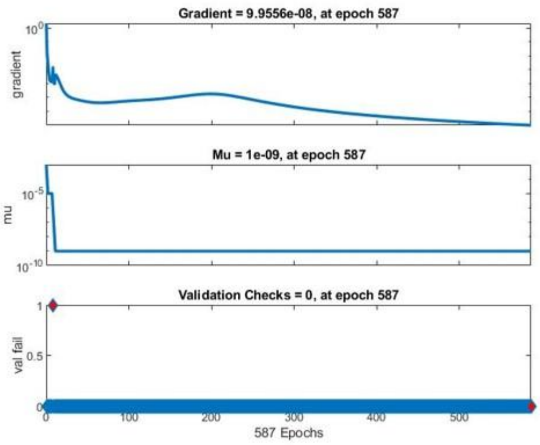

(b) Training state plot.

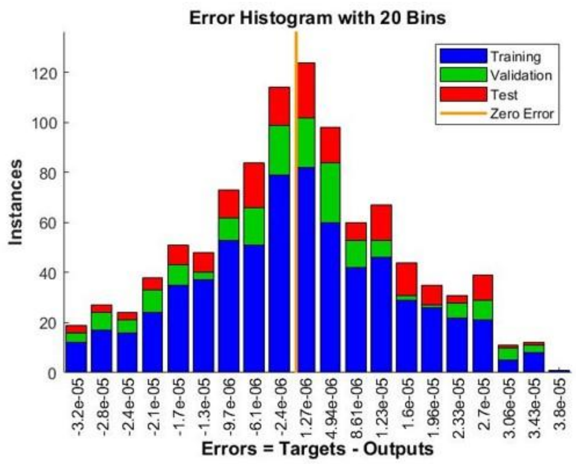

(c) EH plot.

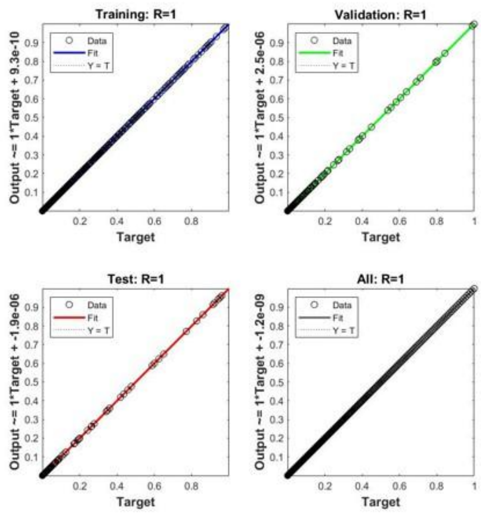

(d) Regression plot.

Figure 4. Performance of $f'(\eta)$ against Bn in the view of the ANN metrics.

Figure 5(a-d) demonstrates the influence of MSEs values, gradient performance, control parameter mu, and EH of control parameter Nr on temperature. The results in Figure 5(a) show that the highest validation efficiency is 1.3039×10^{-10} at the 577 epoch. As seen in Figure 5(b), the gradient is 9.9676×10^{-8} at this point, the validity check remains near zero, and mu is 1×10^{-9}. The reference data and LM-ANN estimates are compared in Figure. 4(c). The results show that there is a substantial correlation between the actual and predicted values, with the lowest errors for testing, validation, and training remaining at about 10^{-4}. The EH for the scenario S2 plot is shown in Figure 5(c). The output-target error, as shown graphically, is 1.67×10^{-6}, which is nearly nil. Furthermore, as shown in Figure 5(d), the anticipated correlation value R reaches the desired value of 1. There are very slight differences between the desired and expected values, as indicated by the error line being around zero. The overall parameter Nr error estimates fall between 10^{-8} and 10^{-4}. The reliability of the Papanastasiou-Bingham HNF model is further supported by these findings.

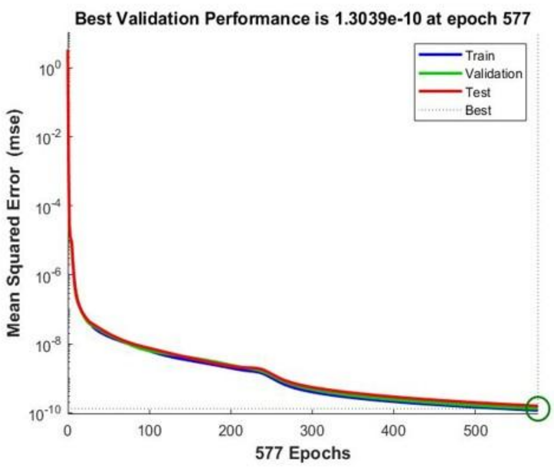

(a) Performance plot.

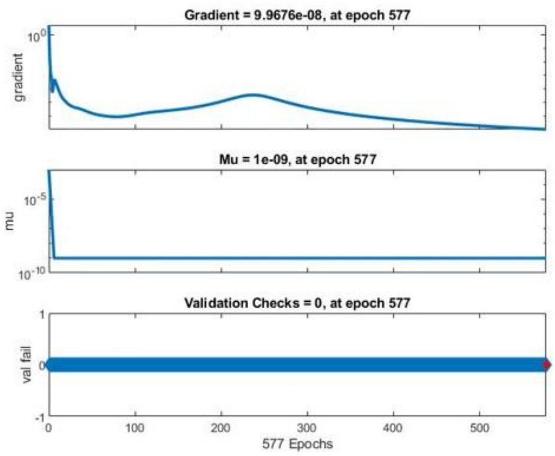

(b) Training state plot.

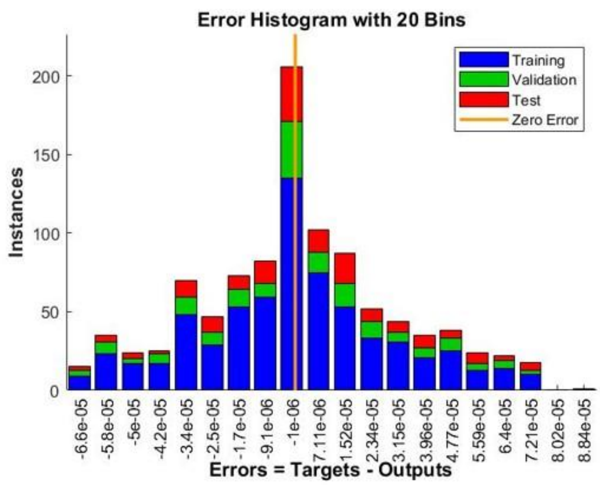

(c) EH plot.

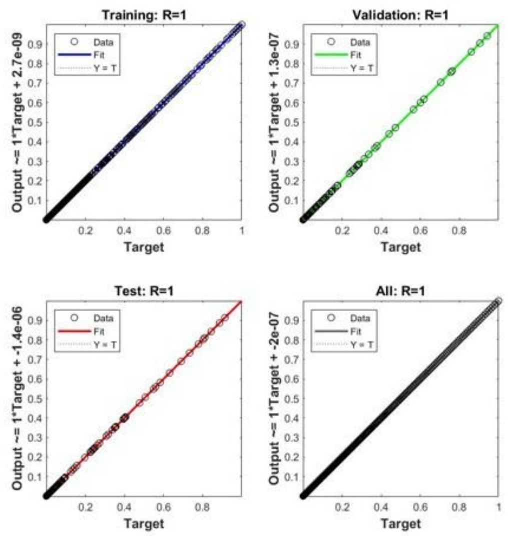

(d) Regression plot.

Figure 5. Performance of $\Theta(\eta)$ against Nr in the view of ANN metrics.

The outcomes of the LM-ANN testing and training for the concentration profile $G(\eta)$ for the third parameter γ_2 are also displayed in Figure 6(a–d). Figure 6(a) shows the best possible validation efficiency 7.0351×10^{-10} at epoch 781, with a gradient of 9.9922×10^{-8}, and Mu set at 1×10^{-8}. At the 781 epoch, as Figure 6(b) illustrates, the validity check is zero. In Figure 6(c), the output-target EH has values close to zero. The coefficient of R^2 reaches the ideal value of 1, indicating that the model successfully and efficiently trains, by offering a good match for the input data with few errors, as shown in Figure 6(d). Every forecast related to γ_2 falls between 10^{-8} and 10^{-4}.

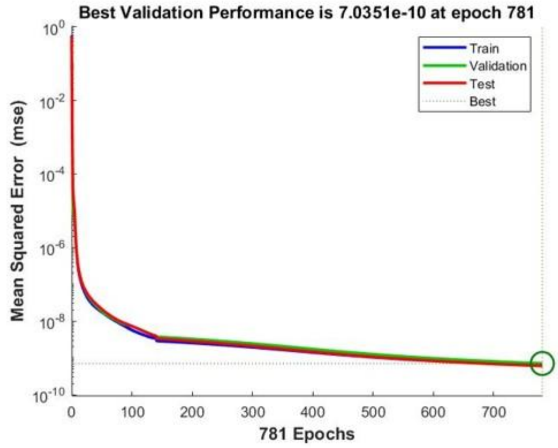

(a) Performance plot.

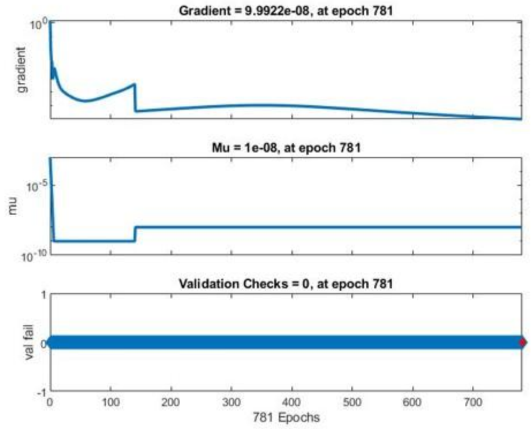

(b) Training state plot.

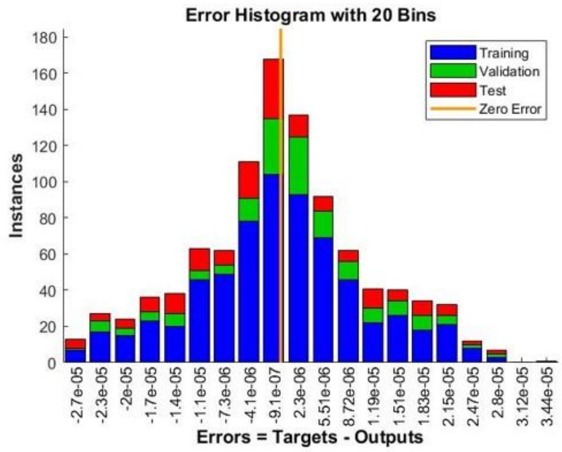

(c) EH plot.

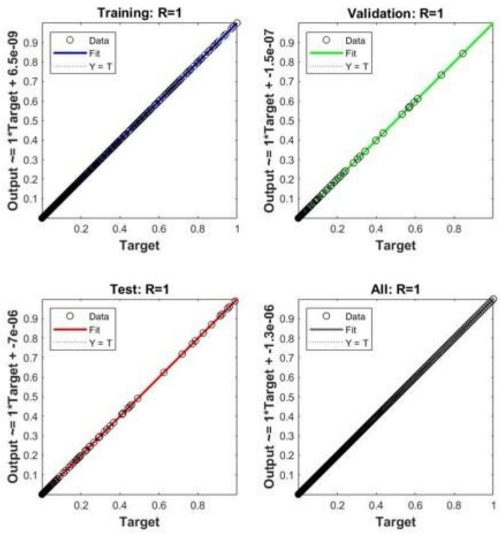

(d) Regression plot.

Figure 6. Performance of $G(\eta)$ against γ_2 in the view of ANN metrics.

The action of Bingham number Bn on velocity $f'(\eta)$ is depicted in Figure 7. A lower velocity within the BL, as a result of a higher Bn, is seen. This occurs because the yield stress to viscous stress ratio is represented by the Bingham number. In contrast to a solo Bingham fluid ($\varphi_{Al_2O_3} = \varphi_{CNT} = 0$), the velocity profile of a Bingham HNF falls more dramatically as Bn grows. This occurs because the yield stress impact imposed by the Bingham parameter is amplified in HNFs ($\varphi_{Al_2O_3} = \varphi_{CNT} = 5\%$) due to the suspended hybrid nanoparticle enhancement of effective viscosity and flow resistance. Physically, the inherent yield stress and the extra drag caused by nanoparticle interactions, the fluid needs a stronger driving force; as a result, the flow field diminishes. Figure 7 shows the mixed convection parameter λ_m uplift velocity profile. The fluid velocity in the BL increases as λ_m increases. Physically, parameter λ_m signifies the proportion of inertial forces (forced convection) to buoyant forces (free convection). A greater number means that buoyancy effects are taking center stage, which thickens the velocity boundary layer and accelerates the flow. The flow profile is higher for solo Bingham compared to Bingham HNF. Figure 8 shows an illustration of a velocity profile $f'(\eta)$ for HNF ($\varphi_{Al_2O_3} = \varphi_{CNT} = 5\%$) and solo Bingham fluid ($\varphi_{Al_2O_3} = \varphi_{CNT} = 0\%$) for different values of the inertia coefficient parameter F_r. The graph shows that as the value of F_r increases, the impact on $f'(\eta)$ decreases. Physically, the inertia is the solid resistance to motion of the fluid; thus, uplifting F_r declines the flow profile. Additionally, it is discovered that the HNF fluid has less velocity than the solo fluid. The velocity profile decreases as the Solutal Grashof γ_1 number rises in the existence of a homogenous chemical reaction (Figure 9). Physically, because of diffusing species within the chemical reaction, the concentration gradient uplift buoyancy force that propels the flow diminishes. The HNF velocity decreases as a result of the chemical reaction counteracting the concentration-driven flow, which is shown by a large γ_1 in this situation (Figure 10).

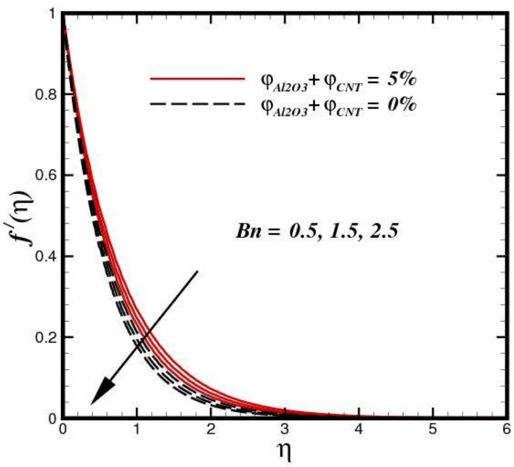

Figure 7. Performance of $f'(\eta)$ against Bn in the view of HNFs and the solo Papanastasiou-Bingham model.

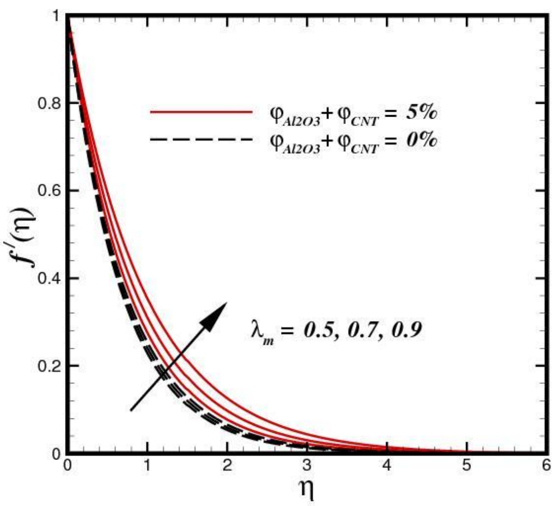

Figure 8. Performance of $f'(\eta)$ against λ_m in the view of HNFs and the solo Papanastasiou-Bingham model.

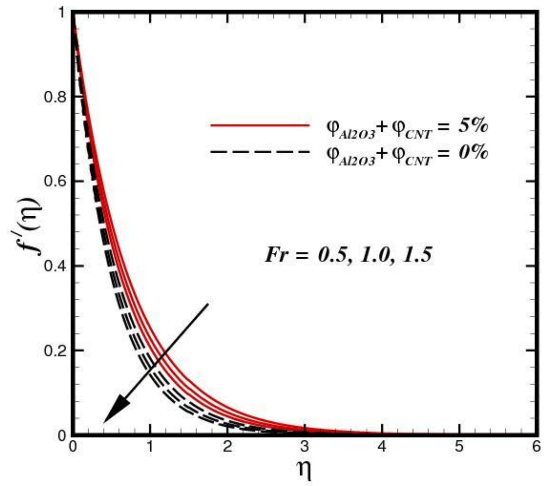

Figure 9. Performance of $f'(\eta)$ against F_r in the view of HNFs and the solo Papanastasiou-Bingham model.

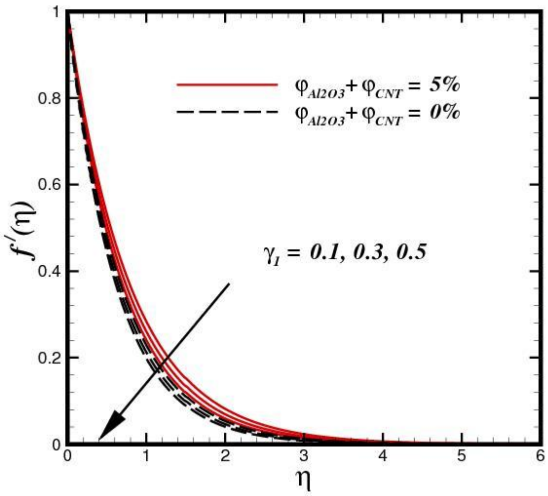

Figure 10. Performance of $f'(\eta)$ against γ_1 in the view of HNFs and the solo Papanastasiou-Bingham model.

Figure 11 displays the impact of the Bingham number Bn on temperature profile $\Theta(\eta)$ for Papanastasiou-Bingham HNF. This figure shows that a Papanastasiou-Bingham HNF ($\varphi_{Al_2O_3} = \varphi_{CNT} = 5\%$) with a greater Bn experiences a decline in velocity. This demonstrates that momentum BL thickness rises for the case of Papanastasiou-Bingham HNF ($\varphi_{Al_2O_3} = \varphi_{CNT} = 5\%$) with higher yield stress because they permit wall momentum to diffuse more quickly than Newtonian fluids. Analyses also show that the HNF thermal BL region is larger than the solo Papanastasiou-Bingham ($\varphi_{Al_2O_3} = \varphi_{CNT} = 0\%$). When comparing HNF to mono Bingham fluid, [57] found a similar pattern. Moreover, Figure 12 is intended to show how the heat transformation rate varies for various thermal radiation parameter Nr adjustments for the HNF and solo Bingham models. For HNF and solo fluid, it is discovered that a higher Nr parameter increases the heat transfer rate. Thermal radiation influences the rate at which energy is transferred to the HNF, raising the HNF temperature. A higher Nr value enables the fluid to receive more heat, which increases the flow of thermal BL thickness and improves temperature distribution. Figures 13 and 14 plot the influences of F_r and D_a, respectively. Because of the increased thermal energy dissipation, F_r and D_a have a greater impact on the temperature profile in a porous medium. Fluid flow is significantly hampered by the porous medium complicated structure of solid matrix and spaces. Internal friction results from this resistance, which is represented by the Darcy and Forchheimer expressions. This friction transforms the fluid kinetic energy into heat energy as it moves through the porous structure. The fluid temperature rises because to the additional heat produced by this action, increasing the BL thickness. Moreover, solo and Papanastasiou-Bingham HNF ($\varphi_{Al_2O_3} = \varphi_{CNT} = 5\%$) exhibit this uplifting behavior, with any slight cooling effects being outweighed by the viscous dissipation from the porous medium.

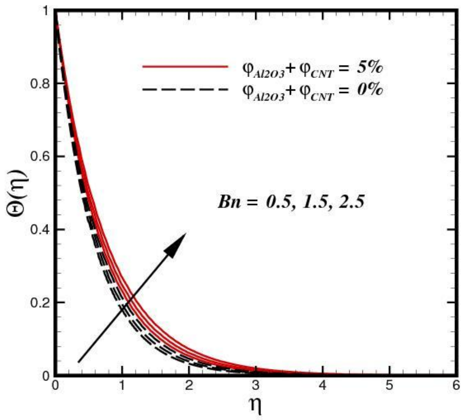

Figure 11. Performance of $\Theta(\eta)$ against Bn in the view of HNFs and the solo Papanastasiou-Bingham model.

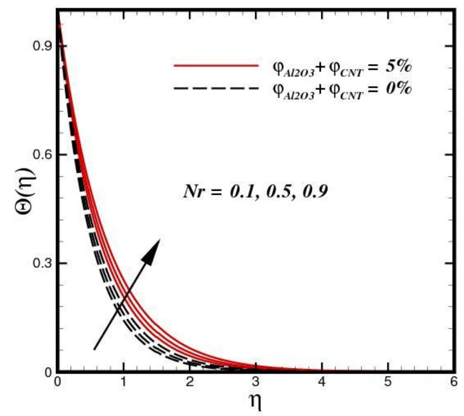

Figure 12. Performance of $\Theta(\eta)$ against Nr in the view of HNFs and the solo Papanastasiou-Bingham model.

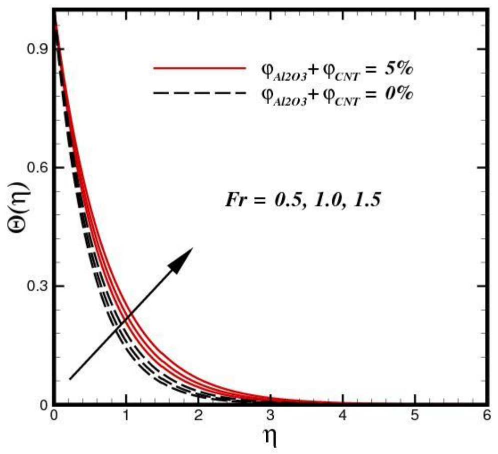

Figure 13. Performance of $\Theta(\eta)$ against F_r in the view of HNFs and the solo Papanastasiou-Bingham model.

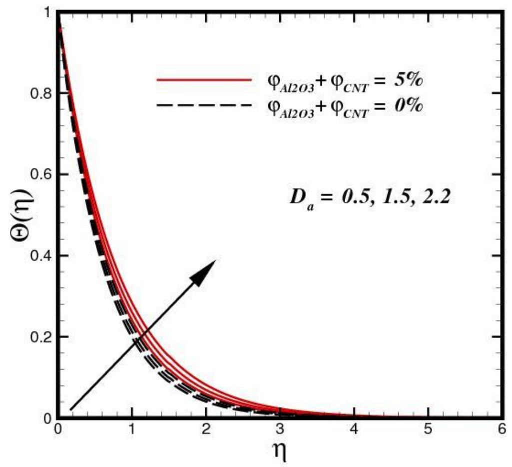

Figure 14. Performance of $\Theta(\eta)$ against D_a in the view of HNFs and the solo Papanastasiou-Bingham model.

In Figures 15 and 16, the effects of solutal Grashof numbers γ_1 and γ_2 resulting from H-H reactions are plotted, respectively. When the chemical reaction takes place evenly throughout the fluid in the case of a homogeneous reaction, the concentration profile $G(\eta)$ decreases as γ_1 increases. This occurs as a result of the reaction consuming the chemical species, which lowers the concentration and hence weakens the buoyant force produced by concentration. The concentration profile also decreases when γ_2 increases in a heterogeneous reaction that takes place on a catalytic surface. Physically, because the species are sucked down by the surface reaction, the concentration within the BL is depleted more quickly, which lowers the concentration overall.

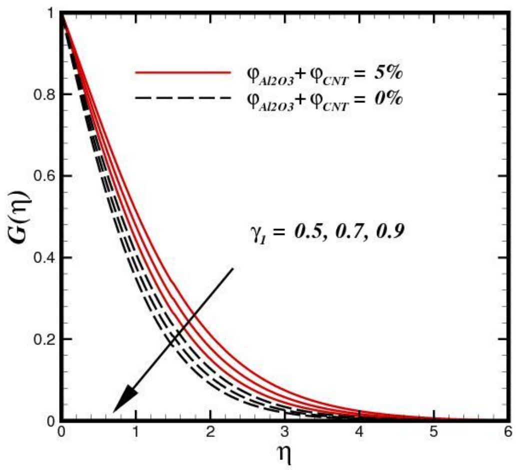

Figure 15. Performance of $\mathrm{G}(\eta)$ against γ_1 in the view of HNFs and the solo Papanastasiou-Bingham model.

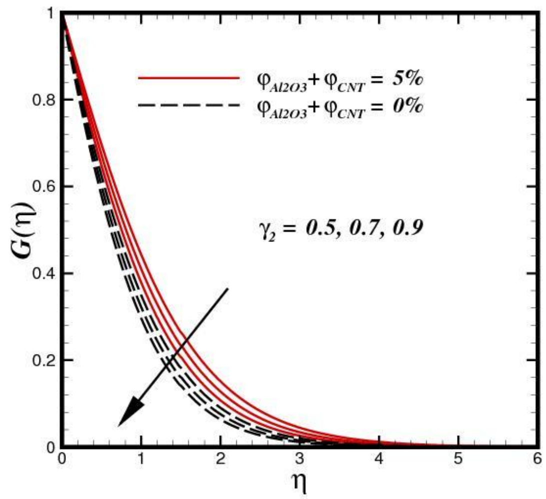

Figure 16. Performance of $\mathrm{G}(\eta)$ against γ_2 in the view of HNFs and the solo Papanastasiou-Bingham model.

Figure 17 plots the effect of Da and Bn on skin friction C_f of the Papanastasiou-Bingham HNF ($\varphi_{Al_2O_3} = \varphi_{CNT} = 5\%$). The skin friction increases with the Da and Bn. More power is needed to start and keep the flow going when the fluid yield stress increases, as indicated by a large Bn. The skin friction rises as a direct result of the increased frictional drag at the surface caused by this increased resistance to motion. Physically, increasing Da lowers the resistivity of the porous medium by raising the permeability K^*. This causes the near-wall fluid velocity to accelerate, steepening the velocity gradient $\frac{\partial \bar{u}}{\partial y}$ at the stretching surface. This directly raises the wall shear stress and increases C_f. Consequently, raising both values raises the flow resistance, which raises skin friction. Figure 18 plots the effects of Bn and λ_m on C_f. The skin friction increases as Bn and

λ_m rises. The fluid velocity within the BL is increased by a positive λ_m, which indicates the dominance of buoyancy forces. A greater velocity gradient is produced at the surface by the faster-moving fluid, increasing the wall shear stress and, eventually, elevating C_f. As a result, both characteristics increase C_f at the surface by distinct physical mechanisms: One by raising the inner resistance and the other by accelerating the flow. Figure 19 plots the effects of Bn and hybrid nanoparticle volume friction on the Nusselt number Nu_x. The fluid heat capacity to transmit heat is directly improved by raising the hybrid nanoparticle volume fraction $\varphi_{Al_2O_3} = \varphi_{CNT} = 5\%$, which increases the fluid thermal conductivity. Physically, because of nanoparticles, random motion produces micro-convection, and higher thermal conductivity boosts the heat transfer rate. On the other hand, parameter Bn has the opposite impact on Nu_x. Convective heat transfer is hampered by higher Bn because it induces a drop in fluid velocity and can lead to a "plug flow" region where the fluid flows as a solid. As a result, although adding nanoparticles enhances the fluid's heat transfer characteristics, increasing Bn reduces this heat transfer efficacy by inhibiting convective flow. Figure 20 illustrates the effects of Bn and the thermal radiation parameter on Nu_x. Heat is immediately transmitted from a surface into the surrounding fluid or air when that surface generates more heat through thermal radiation. Utilizing the fluid convective motion, this effective radiative heat transfer removes the need for heat absorption. As a result of the surface being cooled more efficiently by radiation, the temperature gradient close to the surface decreases. The value of Nu_x falls because it is inversely related to this temperature gradient. In essence, the cooling phenomenon is physically represented by the fluid having to exert less effort to remove the heat. Figure 21, illustrates the effects of Sc and γ_1 on Sherwood number Sh_x. A higher Sc value means that mass diffuses more slowly than momentum, which results in a steeper concentration gradient at the surface and a thinner concentration boundary layer. This increases the rate of mass transfer and raises the Sherwood number. Conversely, concentration gradients cause the Solutal Grashof number γ_1 to increase fluid velocity. More vigorous flow results from a higher γ_1 value, which more successfully removes the chemical species from the surface. Additionally, a steeper concentration gradient at the wall is caused by this enhanced fluid velocity. Another factor that accelerates mass transfer and raises the Sherwood number is the existence of a homogeneous chemical reaction that consumes the species, which further steepens the concentration gradient at the surface. Figure 22 shows the influence of γ_2 and γ_1 on Sherwood number Sh_x. In a H-H chemical reaction, this impact is influenced by both types of reactions. The fluid's homogeneous reaction can serve as an absorbent for the diffusing species, uniformly lowering the concentration of that species. On the surface, the species are consumed by the heterogeneous reaction. By reducing the concentration inside the boundary layer, both processes make the gradient between the fluid's concentration and the surface steeper. The Sherwood number is raised even more by this steeper gradient, which acts as a powerful mass transfer driver. Chemically reacting-driven consumption and concentration-driven buoyancy essentially cooperate to increase the total mass transfer rate.

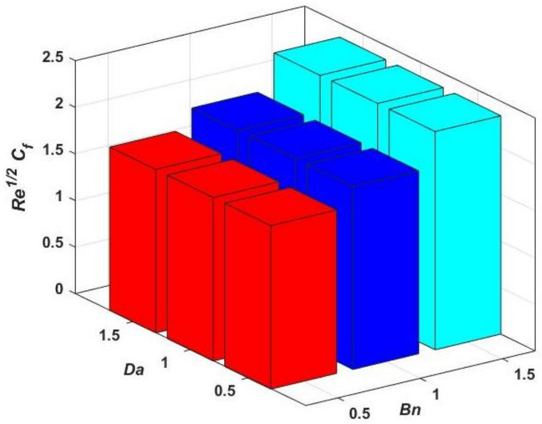

Figure 17. Skin friction performance with varying Da and Bn.

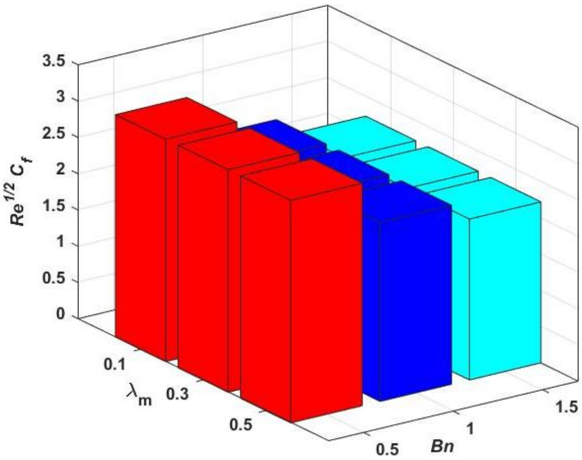

Figure 18. Skin friction performance with varying Bn and λ_m.

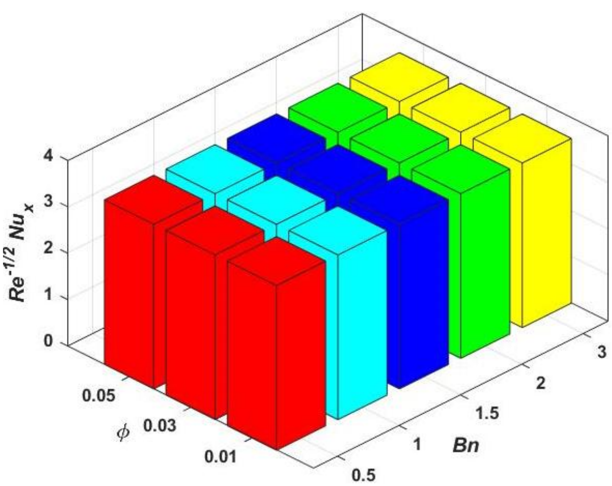

Figure 19. Nusselt performance with varying Bn and φ.

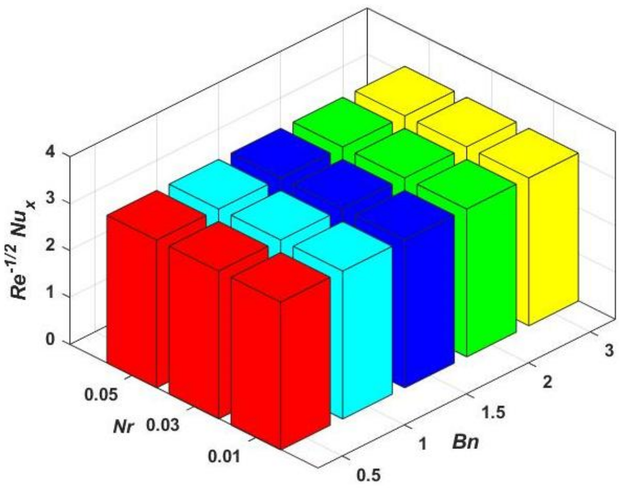

Figure 20. Nusselt performance with varying Bn and Nr.

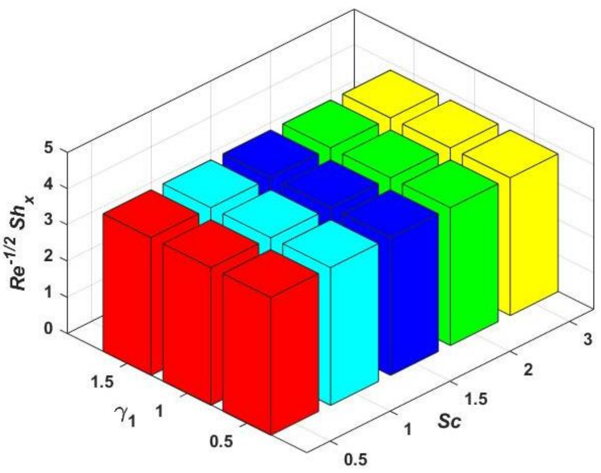

Figure 21. Sherwood performance with varying Sc and γ_1.

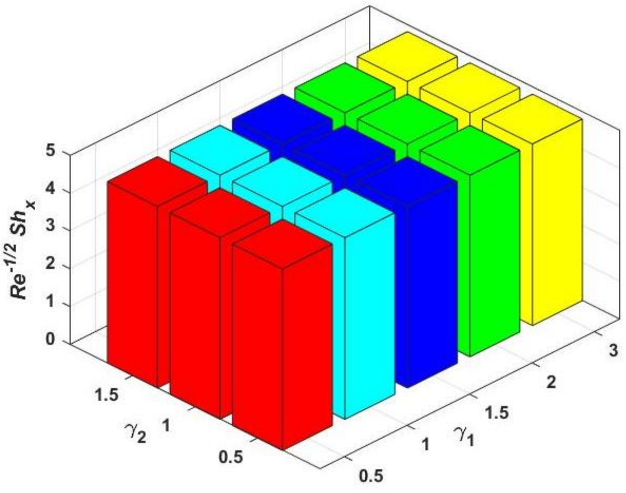

Figure 22. Sherwood performance with varying γ_2 and γ_1.

4. Conclusions

In this study, I explore the heat and mass transportation in the water-based Papanastasiou-Bingham HNF for the 2D Darcy-Forchheimer dissipative flow model over a stretched surface. Two distinct types of nanoparticles, CNTs (platelet) and Al_2O_3 (spherical), are used to theoretically and systematically study the impacts of a H-H chemical reaction in a flow model. Heat dissipation due to porous media and H-H chemical reactions are taken into account. The PDE describes the HNF flow patterns by converting them into ODEs using a conversion method, and the datasets are obtained by solving the ODEs using the RK45 numerical solver. The HNF model solutions are then approximated using the reference dataset and the LM-ANN technique. The following conclusions are drawn:

- Velocity of Papanastasiou-Bingham HNF is a decreasing function of Bn, F_r, and γ_1, while an opposite trend is observed for λ_m. Furthermore, the flow of Papanastasiou-Bingham HNF shows dominant behavior compared to solo Papanastasiou-Bingham fluid.
- Temperature escalates with Bn, F_r, Nr, and D_a. Moreover, due to high thermal conductivity of CNTs and Al_2O_3, the temperature of Papanastasiou-Bingham HNF is much higher than Papanastasiou-Bingham fluid.
- Concentration of the Papanastasiou-Bingham HNF is decreasing function of novel parameters γ_1 and γ_2.
- Skin friction increases with $Da,$ λ_m, and Bn. The viscoplasticity of the fluid has a major impact on skin friction. Moreover, shear stress increases for the wall uplift as Bn rises. As a result, viscoplastic fluids with higher yield stress force the surface to be under more shear stress. Because of the fluid viscoplastic rheological nature, the geometries and surfaces need to be designed with sufficient strength to handle additional shear stress.
- The wall shear stress increases when, D_a and Bn increase. Additionally, it is seen that the surface of the Darcy porous media experiences increased shear stress due to the viscoplastic fluid.
- The viscoplastic fluid containing hybrid nanoparticles shows high wall stress, heat, and mass fluxes, according to computational experiments. The visualizations have shown that two nanoparticles dispersed in a viscoplastic fluid impose higher shear stress than a viscoplastic fluid functioning individually.
- The machine learning curve MSE of roughly 10^{-9} indicates that the LM-ANN results match the smallest error. In almost 90% of the cases, the corresponding dynamics are centered about the zero line segment of the histograms, and the regression coefficient R^2 is nearly 1.

This work can be extended for immediate prescriptive control in dynamic flow geometries by fusing data-driven artificial intelligence with physical modeling to create new avenues for effective, realistic simulations of complex non-Newtonian flows in industrial, medical, and nanotechnology systems.

4.1. Limitation of the study

In this study, I eliminate three-dimensional and transient effects, limiting the study to two-dimensional, steady, incompressible flow over a stretching sheet. Stiff equations may be difficult for the RKF-45 numerical solver to solve, necessitating unfeasibly small steps and possibly failing close to singularities. With training restricted to 800 samples and a single hidden layer of ten neurones, the ANN predictions are data-dependent and might not generalize outside the selected parameter ranges. In addition to ignoring MHD effects, slip conditions, and temperature-dependent viscosity fluctuations, the model assumes constant thermophysical characteristics and identical diffusion coefficients ($\beta = 1$) for chemical species. Furthermore, since the results are based only on computational and numerical benchmarks rather than physical observations, no experimental confirmation is offered.

Use of Generative-AI tools declaration

The author declares he has not used Artificial Intelligence (AI) tools in the creation of this article.

Conflict of interest

The author of this manuscript has no conflict of interest.

References

1. C. R. Beverly, R. I. Tanner, Numerical analysis of three-dimensional Bingham plastic flow, *J. Non-Newtonian Fluid Mech.*, **42** (1992), 85–115. http://doi.org/10.1016/0377-0257(92)80006-J
2. G. H. Tang, S. B. Wang, P. X. Ye, W. Q. Tao, Bingham fluid simulation with the incompressible lattice Boltzmann model, *J. Non-Newtonian Fluid Mech.*, **166** (2011), 145–151. https://doi.org/10.1016/j.jnnfm.2010.11.005
3. Eugene C. Bingham, *Fluidity and plasticity*, Mcgraw-Hill Book Company Inc., 1922.
4. R. B. Bird, G. C. Dai, B. J. Yarusso, The rheology and flow of viscoplastic materials, *Rev. Chem. Eng.*, **1** (1983), 1–70. https://doi.org/10.1515/revce-1983-0102
5. S. Ahmad, D. Liu, B. M. Cham, S. Yang, S.-L. Sun, Exploring conjugate heat transfer in Bingham fluid flow: a 3D computational approach incorporating double diffusion and the Papanastasiou model, *Appl. Therm. Eng.*, **273** (2025), 126500. https://doi.org/10.1016/j.applthermaleng.2025.126500
6. T. C. Papanastasiou, Flows of materials with yield, *J. Rheol.*, **31** (1987), 385–404. https://doi.org/10.1122/1.549926
7. O. Turan, S. Yigit, N. Chakraborty, Numerical investigation of mixed convection of Bingham fluids in cylindrical enclosures with heated rotating top wall, *Int. J. Heat Mass Tran.*, **108** (2017), 1850–1869. https://doi.org/10.1016/j.ijheatmasstransfer.2017.01.034
8. G. W. Parshall, Industrial applications of homogeneous catalysis. A review, *Journal of Molecular Catalysis*, **4** (1978), 243–270. https://doi.org/10.1016/0304-5102(78)85023-8
9. J. Heveling, Heterogeneous catalytic chemistry by example of industrial applications, *J. Chem. Educ.*, **89** (2012), 1530–1536. https://doi.org/10.1021/ed200816g
10. M. J. Climent, A. Corma, S. Iborra, Homogeneous and heterogeneous catalysts for multicomponent reactions, *RSC Adv.*, **2** (2012), 16–58. https://doi.org/10.1039/C1RA00807B

11. C. Amatore, M. Gareil, J. M. Savéant, Homogeneous vs. heterogeneous electron transfer in electrochemical reactions: application to the electrohydrogenation of anthracene and related reactions, *Journal of Electroanalytical Chemistry and Interfacial Electrochemistry*, **147** (1983), 1–38. https://doi.org/10.1016/S0022-0728(83)80054-0
12. T. H. Alarabi, A. M. Rashad, A. Mahdy, Homogeneous–heterogeneous chemical reactions of radiation hybrid nanofluid flow on a cylinder with Joule heating: nanoparticles shape impact, *Coatings*, **11** (2021), 1490. https://doi.org/10.3390/coatings11121490
13. M. Ramzan, H. Chaudhry, H. A. S. Ghazwani, S. Kadry, N. Shahmir, M. Abbas, et al., Impact of homogeneous–heterogeneous reactions on nanofluid flow through a porous channel – A Tiwari and Das model application, *Numer. Heat Trans. A: Appl.*, **85** (2024), 1317–1330. https://doi.org/10.1080/10407782.2023.2201484
14. Hashim, S. Rehman, S. Alshammari, A. Osman Ibrahim, N. Ullah, Entropy production with the flow of nanomaterials through the permeable stretched surface with heterogeneous–homogenous chemical reaction, *Nanoscale Adv.*, **5** (2023), 5580–5593. https://doi.org/10.1039/D3NA00639E
15. S. Feng, R. Su, Synthetic chemistry in flow: from photolysis & homogeneous photocatalysis to heterogeneous photocatalysis, *ChemSusChem*, **17** (2024), e202400064. https://doi.org/10.1002/cssc.202400064
16. S. Jena, K. Swain, S. M. Ibrahim, P. Sreenivasulu, G. Lorenzini, Three-dimensional MHD rotating flow of radiative nanofluid over a stretched sheet with homogeneous-heterogeneous chemical reactions, *J. Eng. Thermophys.*, **33** (2024), 336–353. https://doi.org/10.1134/S1810232824020097
17. A. K. Sharma, A. K. Tiwari, A. R. Dixit, Progress of nanofluid application in machining: a review, *Mater. Manuf. Process.*, **30** (2015), 813–828. https://doi.org/10.1080/10426914.2014.973583
18. M. Zulfiqar, M. B. Arain, M. Zubair, Usman, H. Alhazmi, A numerical investigation of heat and mass transfer in the bioconvective Oldroyd B nanofluid flow through the porous stretching Riga surface with gyrotactic microorganism, *Case Stud. Therm. Eng.*, **72** (2025), 106431. https://doi.org/10.1016/j.csite.2025.106431
19. S. U. S. Choi, J. A. Eastman, Enhancing thermal conductivity of fluids with nanoparticles, In: *ASME International Mechanical Engineering Congress & Exposition*, November 12–17, 1995, San Francisco.
20. Preeti, O. Ojjela, Numerical investigation of heat transport in Alumina–Silica hybrid nanofluid flow with modeling and simulation, *Math. Comput. Simulat.*, **193** (2022), 100–122. https://doi.org/10.1016/j.matcom.2021.09.022
21. A. H. Ganie, Z. Mahmood, U. Khan, M. Y. Almusawa, Impact of nonlinear thermal radiation on three-dimensional unsteady flow of carbon nanotube-suspended nanofluid with different length and radius over a stretching surface, *Int. J. Mod. Phys. C*, **35** (2024), 2440001. https://doi.org/10.1142/S0129183124400011
22. X. Sun, L. Xu, H. Yuan, G. Wang, B. Maleki, Boosted conversion of restaurant waste oil into biodiesel using Fe_3O_4@UiO-66-NH_2 magnetic heterogeneous nanocatalyst and its application on the diesel engine: optimization via RSM, *Renew. Energ.*, **223** (2024), 120007. https://doi.org/10.1016/j.renene.2024.120007

23. M. Muneeshwaran, G. Srinivasan, P. Muthukumar, C.-C. Wang, Role of hybrid-nanofluid in heat transfer enhancement – A review, *Int. Commun. Heat Mass*, **125** (2021), 105341. https://doi.org/10.1016/j.icheatmasstransfer.2021.105341
24. J. Sarkar, P. Ghosh, A. Adil, A review on hybrid nanofluids: recent research, development and applications, *Renewable and Sustainable Energy Reviews*, **43** (2015), 164–177. https://doi.org/10.1016/j.rser.2014.11.023
25. A. Hafeez, D. Liu, A. Khalid, MHD flow of radiative hybrid nanofluid across a wedge influenced by melting heat transfer: Engineering application, *Alex. Eng. J.*, **122** (2025), 18–27. https://doi.org/10.1016/j.aej.2025.03.018
26. B. Jalili, P. M. Zar, D. Liu, C.-H. Ji, P. Jalili, M. A. H. Abdelmohimen, et al., Thermal study of MHD hybrid nano fluids confined between two parallel sheets: shape factors analysis, *Case Stud. Therm. Eng.*, **63** (2024), 105229. https://doi.org/10.1016/j.csite.2024.105229
27. M. Nasir, M. S. Kausar, D. khan, H. E. Hashim, M. Suhail, M. Rabih, Numerical investigation of hydrogen diffusion in radiative MHD nanofluid mixed convection flow over a stretching wedge, *Int. J. Hydrogen Energ.*, **240** (2026), 155513. https://doi.org/10.1016/j.ijhydene.2026.155513
28. M. Kurucan, M. Özbaltan, Z. Yetgin, A. Alkaya, Applications of artificial neural network based battery management systems: a literature review, *Renewable and Sustainable Energy Reviews*, **192** (2024), 114262. https://doi.org/10.1016/j.rser.2023.114262
29. A. Kaveh, Artificial intelligence: background, applications and future, In: *Applications of artificial neural networks and Machine Learning in Civil Engineering*, Cham: Springer, 2024, 1–53. https://doi.org/10.1007/978-3-031-66051-1_1
30. M. B. Arain, D. Hussain, F. A. M. Al-Yarimi, S. Shaheen, J. Hu, Intelligent predictive networks of swimming of microorganism for tangent hyperbolic fluid flow with heat and mass transfer and Thompson and Troian slip conditions using Levenberg-Marquardt algorithm, *Eng. Appl. Artif. Intel.*, **152** (2025), 110749. https://doi.org/10.1016/j.engappai.2025.110749
31. N. S. Akbar, T. Zamir, J. Akram, T. Noor, T. Muhammad, Simulation of hybrid boiling nano fluid flow with convective boundary conditions through a porous stretching sheet through Levenberg Marquardt artificial neural networks approach, *Int. J. Heat Mass Tran.*, **228** (2024), 125615. https://doi.org/10.1016/j.ijheatmasstransfer.2024.125615
32. S. Z. H. Shah, A. Ayub, S. Bhatti, U. Khan, A. Ishak, E.-S. M. Sherif, et al., Aspects of inclined magnetohydrodynamics and heat transfer in a non-Newtonian tri-hybrid bio-nanofluid flow past a wedge-shaped artery utilizing artificial neural network scheme, *Z. Angew. Math. Mech.*, **104** (2024), e202400278. https://doi.org/10.1002/zamm.202400278
33. F. Alimi, S. Rehman, M. Bouzidi, F. Asiri, T. Saidani, V. Tirth, Numerical and artificial neural network framework for predicating MHD radiative flow and heat transfer of hybrid nanofluid with Cattaneo-Christov theory, *Case Stud. Therm. Eng.*, **72** (2025), 106311. https://doi.org/10.1016/j.csite.2025.106311
34. R. R. Sahoo, V. Kumar, Development of a new correlation to determine the viscosity of ternary hybrid nanofluid, *Int. Commun. Heat Mass*, **111** (2020), 104451. https://doi.org/10.1016/j.icheatmasstransfer.2019.104451
35. M. D. Kumar, C. S. K. Raju, K. Sajjan, E. R. El-Zahar, N. A. Shah, Linear and quadratic convection on 3D flow with transpiration and hybrid nanoparticles, *Int. Commun. Heat Mass*, **134** (2022), 105995. https://doi.org/10.1016/j.icheatmasstransfer.2022.105995

36. M. Nasir, M. S. Kausar, M. Waqas, N. Zamri, M. Jameel, R. F. Rashid, et al., Numerical simulations for chemically reactive Darcy-Forchheimer driven viscoplastic nanomaterial subjected to magnetic dipole and gyrotactic microorganisms, *Tribol. Int.*, **204** (2025), 110431. https://doi.org/10.1016/j.triboint.2024.110431
37. M. Ahmed, M. Nawaz, Numerical investigation on heat and mass transport enhancement in viscoplastic hybrid nanofluid using Bingham-Papanastasiou rheological theory, *Int. Commun. Heat Mass*, **168** (2025), 109448. https://doi.org/10.1016/j.icheatmasstransfer.2025.109448
38. M. I. Afridi, M. P. Mkhatshwa, M. Qasim, A. J. Chamkha, Non-similar solutions for Darcy-Forchheimer flow with multiple dissipative mechanisms: a spectral collocation approach, *Chinese J. Phys.*, **98** (2025), 254–276. https://doi.org/10.1016/j.cjph.2025.08.014
39. M. Nasir, M. S. Kausar, D. khan, H. E. Hashim, M. Suhail, M. Rabih, Numerical investigation of hydrogen diffusion in radiative MHD nanofluid mixed convection flow over a stretching wedge, *Int. J. Hydrogen Energ.*, **240** (2026), 155513. https://doi.org/10.1016/j.ijhydene.2026.155513
40. Z. Shah, A. A. Pasha, M. Nasir, M. S. Basingab, M. Zafar, A. Z. Hameed, et al., Thermally magnetized Darcy–Forchheimer Eyringen micropolar material subject to chemical kinetics: a machine learning analysis, *Chem. Eng. J. Adv.*, **25** (2026), 100992. https://doi.org/10.1016/j.ceja.2025.100992
41. H.-X. Bao, M. B. Arain, S. Shaheen, H. I. Khan, Usman, M. Inc, et al., Boundary-layer flow of heat and mass for Tiwari-Das nanofluid model over a flat plate with variable wall temperature, *Therm. Sci.*, **26** (2022), 39–47. https://doi.org/10.2298/TSCI22S1039B
42. S. Khan, M. I. Asjad, F. Maiz, Artificial neural networks computing for heat transfer flow of hybrid nanofluid in rectangular geometry, *Computers in Biology and Medicine*, **194** (2025), 110475. https://doi.org/10.1016/j.compbiomed.2025.110475
43. M. Bilal, M. Farooq, H. Ahmad, I. Ullah, M. M. Alam, Mathematical simulation of tangent hyperbolic nanofluid flow coupled with homogenous/heterogeneous chemical reaction by using Levenberg–Marquardt back propagation over a Riga plate, *J. Therm. Anal. Calorim.*, **150** (2025), 2795–2809. https://doi.org/10.1007/s10973-024-13554-1
44. M. Nasir, A. B. M. Ali, M. Waqas, I. A. Ahmed, Magnetized transport of chemically reactive viscoplastic nanomaterials with dual diffusion driven by a rotating disk, *Nanotechnol. Rev.*, **15** (2026), 20250273. https://doi.org/10.1515/ntrev-2025-0273
45. S. R. Mishra, P. K. Pattnaik, R. Baithalu, P. K. Ratha, S. Panda, Predicting heat transfer Performance in transient flow of CNT nanomaterials with thermal radiation past a heated spinning sphere using an artificial neural network: a machine learning approach, *Partial Differential Equations in Applied Mathematics*, **12** (2024), 100936. https://doi.org/10.1016/j.padiff.2024.100936
46. Y. Jiang, X. Zhou, Y. Wang, Effects of nanoparticle shapes on heat and mass transfer of nanofluid thermocapillary convection around a gas bubble, *Microgravity Sci. Technol.*, **32** (2020), 167–177. https://doi.org/10.1007/s12217-019-09757-z
47. M. M. Maskeen, A. Zeeshan, O. U. Mehmood, M. Hassan, Heat transfer enhancement in hydromagnetic alumina–copper/water hybrid nanofluid flow over a stretching cylinder, *J. Therm. Anal. Calorim.*, **138** (2019), 1127–1136. https://doi.org/10.1007/s10973-019-08304-7

48. A. Ali, M. N. Aslam, M. S. Junaid, A. Al-Zubaidi, T. Sohail, S. T. Saeed, Thermal stratification of Darcy-Forchheimer nano-fluid flow with cattaneo-christov heat flux over a riga plate: a mathematical analysis, *Case Stud. Therm. Eng.*, **74** (2025), 106794. https://doi.org/10.1016/j.csite.2025.106794
49. S. Al Arni, Z. Shah, S. Mehmood, H. Iqbal, M. Jawaid, A. magdich, et al., Machine learning-based numerical analysis of ternary hybrid nanofluid flow with Cattaneo-Christov heat flux, *Case Stud. Therm. Eng.*, **74** (2025), 106861. https://doi.org/10.1016/j.csite.2025.106861
50. S. Rehman, Hashim, S. Alqahtani, S. Alshehery, M. Boujelbene, Modelling heat-mass transport for MHD Eyring-Powell hybrid nanofluid over an expanding surface laden by autocatalytic chemical reaction and nanoparticles diffusion, *Adv. Eng. Softw.*, **186** (2023), 103549. https://doi.org/10.1016/j.advengsoft.2023.103549
51. G. H. Tang, S. B. Wang, P. X. Ye, W. Q. Tao, Bingham fluid simulation with the incompressible lattice Boltzmann model, *J. Non-Newtonian Fluid Mech.*, **166** (2011), 145–151. https://doi.org/10.1016/j.jnnfm.2010.11.005
52. E. Mitsoulis, R. R. Huilgol, Entry flows of Bingham plastics in expansions, *J. Non-Newtonian Fluid Mech.*, **122** (2004), 45–54. https://doi.org/10.1016/j.jnnfm.2003.10.007
53. S. Rehman, W. Ahmed, S. NASR, Optimization of MHD Jeffrey-Hamel flow in convergent–divergent channels with slip and viscous-dissipation: vorticity–stream-function analysis of flow reversal and heat transfer, *J. Taibah Univ. Sci.*, **19** (2025), 2548630. https://doi.org/10.1080/16583655.2025.2548630
54. M. Ahmed, M. Nawaz, Numerical investigation on heat and mass transport enhancement in viscoplastic hybrid nanofluid using Bingham-Papanastasiou rheological theory, *Int. Commun. Heat Mass*, **168** (2025), 109448. https://doi.org/10.1016/j.icheatmasstransfer.2025.109448
55. A. Akbar, H. Ullah, M. A. Z. Raja, K. S. Nisar, S. Islam, M. Shoaib, A design of neural networks to study MHD and heat transfer in two phase model of nano-fluid flow in the presence of thermal radiation, *Waves in Random and Complex Media*, **36** (2026), 157–180. https://doi.org/10.1080/17455030.2022.2152905
56. M. I. Khan, M. Waqas, T. Hayat, A. Alsaedi, A comparative study of Casson fluid with homogeneous-heterogeneous reactions, *J. Colloid Interf. Sci.*, **498** (2017), 85–90. https://doi.org/10.1016/j.jcis.2017.03.024
57. L. F. Shampine, I. Gladwell, S. Thompson, *Solving ODEs with MATLAB*, Cambridge University Press, 2003.
58. R. A. Van Gorder, K. Vajravelu, On the selection of auxiliary functions, operators, and convergence control parameters in the application of the homotopy analysis method to nonlinear differential equations: a general approach, *Commun. Nonlinear Sci.*, **14** (2009), 4078–4089. https://doi.org/10.1016/j.cnsns.2009.03.008
59. A. Ishak, R. Nazar, I. Pop, Boundary layer flow and heat transfer over an unsteady stretching vertical surface, *Meccanica*, **44** (2009), 369–375. https://doi.org/10.1007/s11012-008-9176-9
60. W. Jamshed, S. Uma Devi S, R. Safdar, F. Redouane, K. S. Nisar, M. R. Eid, Comprehensive analysis on copper-iron (II, III)/oxide-engine oil Casson nanofluid flowing and thermal features in parabolic trough solar collector, *J. Taibah Univ. Sci.*, **15** (2021), 619–636. https://doi.org/10.1080/16583655.2021.1996114

61. M. Benkhedda, T. Boufendi, T. Tayebi, A. J. Chamkha, Convective heat transfer performance of hybrid nanofluid in a horizontal pipe considering nanoparticles shapes effect, *J. Therm. Anal. Calorim*, **140** (2020), 411–425. https://doi.org/10.1007/s10973-019-08836-y
62. S. Mehmood, S. U. Rehman, Simulation and accurate prediction of unsteady nonlinear convection flow by artificial neural network using numerical data, *Phys. Fluids*, **37** (2025), 043122. https://doi.org/10.1063/5.0264294

AIMS Press